Supplementary Information

Multicolor cathodoluminescence imaging of single lanthanide nanoparticles

Sohaib Abdul Rehman[1,2,*], Jeremy B. Conway[1,2,*], Amy Nichols[1,2], Edward R. Soucy[3], Amanda Dee[1,2], Kristal Stevens[1,2], Simon Merminod[1,2], Isabella MacNaughton[1,2], Abigail Curtis[1,2], and Maxim B. Prigozhin[1,2,†]

[1]Department of Molecular and Cellular Biology, Harvard University, Cambridge, MA 02138 USA

[2]John A. Paulson School of Engineering and Applied Sciences, Harvard University, Cambridge, MA 02138 USA

[3]Center for Brain Science, Harvard University Cambridge, MA 02138 USA

*These authors contributed equally to this work.

[†]Corresponding author: maxim_prigozhin@harvard.edu

Table of Contents

Supplementary Note 1. Synthesis of LNPs 3
Supplementary Note 2. Nanoparticle sample preparation 5
Supplementary Note 3. Impact of dopant concentration on LNP brightness 6
Supplementary Note 4. CL detection system 7
Supplementary Note 5. Image acquisition 8
Supplementary Note 6. Impact of field of view on nonlocal CL signal 9
Supplementary Note 7. Impact of atomic number on nonlocal CL signal 10
Supplementary Note 8. Can X-rays cause nonlocal CL? 11
Supplementary Note 9. Nonlocal excitation when imaging different nanoparticles 13
Supplementary Note 10. Nonlocal CL signal on different substrates 14
Supplementary Note 11. SEM imaging of single LNPs close to aggregates 16
Supplementary Note 12. Two-color and three-color imaging 17
Supplementary Note 13. Automated dopant assignment in multicolor samples 19
Supplementary Note 14. Impact of nonlocal excitation on single-particle CL 22
Supplementary Note 15. Image analysis for single-particle characterization 23
Supplementary Note 16. Spectrum of holmium chloride 26
Supplementary Note 17. Optimizing electron beam current for CL imaging 26
Supplementary Note 18. Optimizing electron beam energy for CL imaging 27
Supplementary Note 19. Background from Si substrate 31
Supplementary Note 20. $NaGdF_4$ nanocrystals as a control sample 32
Supplementary Note 21. Relationship between CL signal and LNP size 34
Supplementary Note 22. Single-particle CL spectra 35
Supplementary Note 23. Electrobleaching 36
Supplementary Note 24. Imaging single LNPs in a biological sample 38
Supplementary Note 25. Impact of plasma on the brightness of LNPs 39
Supplementary Note 26. Nonlocal excitation from the SEM chamber 39
Supplementary Note 27. Dipole emission on different substrates 40
Supplementary Note 28. Repeatability 41
Supplementary Note 29. Crosstalk between LNPs in dense samples 41
Supplementary Note 30. Summary of imaging conditions from main text 44

Supplementary Note 1. Synthesis of LNPs

Materials: Oleic acid (Sigma-Aldrich, Cat# 364525-1L, 90%, technical grade), 1-octadecene (SigmaAldrich, Cat# O806-1L, 90%, technical grade), rare-earth chlorides [yttrium trichloride hexahydrate (Sigma-Aldrich, Cat# 464317-25G, 99.99%), samarium trichloride hexahydrate (Sigma-Aldrich, Cat# 204277-5G, ≥99.99%), gadolinium trichloride hexahydrate (Sigma-Aldrich, Cat# 203289-25G, 99.999%), terbium trichloride hexahydrate (Sigma-Aldrich, Cat# 212903-5G, 99.9%), dysprosium trichloride hexahydrate (Sigma-Aldrich, Cat# 289272-25G, 99.9%), holmium trichloride hexahydrate (Sigma-Aldrich, Cat# 289213-5G, 99.9%), lutetium trichloride hexahydrate (Sigma-Aldrich, Cat# 542075-5G, ≥99.99%)], sodium hydroxide (Sigma-Aldrich, Cat# 221465-500G, ACS Reagent, ≥97.0%, pellets), methanol (Sigma-Aldrich, Cat# 34860-1L-R, ≥99.9%), ammonium fluoride (Sigma-Aldrich, Cat# 216011-100G, ACS Reagent, ≥98.0%), n-hexane (Sigma-Aldrich, Cat# HX0302-3, 95%), ethanol (Ethyl alcohol, Sigma-Aldrich, Cat# 459844-1L, 200 proof, ACS Reagent, ≥99.5%).

Protocol: $NaSmF_4$, $NaTbF_4$, $NaDyF_4$, $NaHoF_4$, and $NaGdF_4$ nanocrystals were synthesized by the coprecipitation method and based on previously reported protocols[1–3]. 0.5 mmol of the appropriate lanthanide chloride hydrate was combined with 3 mL of oleic acid and 7.5 mL of 1-octadecene in a 100 mL three-neck round-bottom flask. The flask was connected to a Schlenk line, with a heating mantle placed underneath and a thermocouple inserted into the flask through a vacuum-tight adapter. Both the heating mantle and the thermocouple were controlled by the Digi-Sense TC9600 temperature control module. Flask contents were stirred continuously using a magnetic egg-shaped stir bar. The reaction was placed under vacuum and the temperature was set to 160 °C for 30 min. The heating mantle was removed, and the solution was cooled to <30 °C, then exposed to air. Next, 1 M sodium hydroxide in methanol and 0.4 M ammonium fluoride in methanol were sonicated to homogeneity separately. A nucleation precursor solution was prepared by adding 1.25 mL of 1 M sodium hydroxide to 5 mL of 0.4 M ammonium fluoride. The resulting precursor solution was vortexed for 10 s and added dropwise to the lanthanide oleate solution in the three-neck round-bottom flask. The reaction was mixed for 60 min while exposed to air at room temperature. Methanol was evaporated by increasing the temperature to 70 °C, and the reaction temperature was maintained between 70 °C and 80 °C for 30 min while exposed to air. Then, for the nanocrystal growth step, the reaction

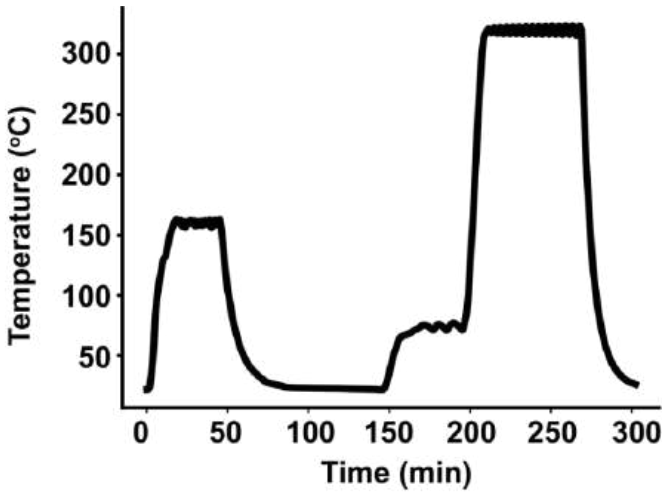

Supplementary Figure 1: LNP synthesis temperature profile. Typical temperature profile of a lanthanide nanocrystal synthesis reaction measured using a thermocouple. The thermocouple was placed in an NMR tube inserted into the round-bottom reaction flask through a vacuum-tight adapter. Thermocouple measurements were recorded using a Digi-Sense TC9600 temperature controller. Source data provided as a Source Data file.

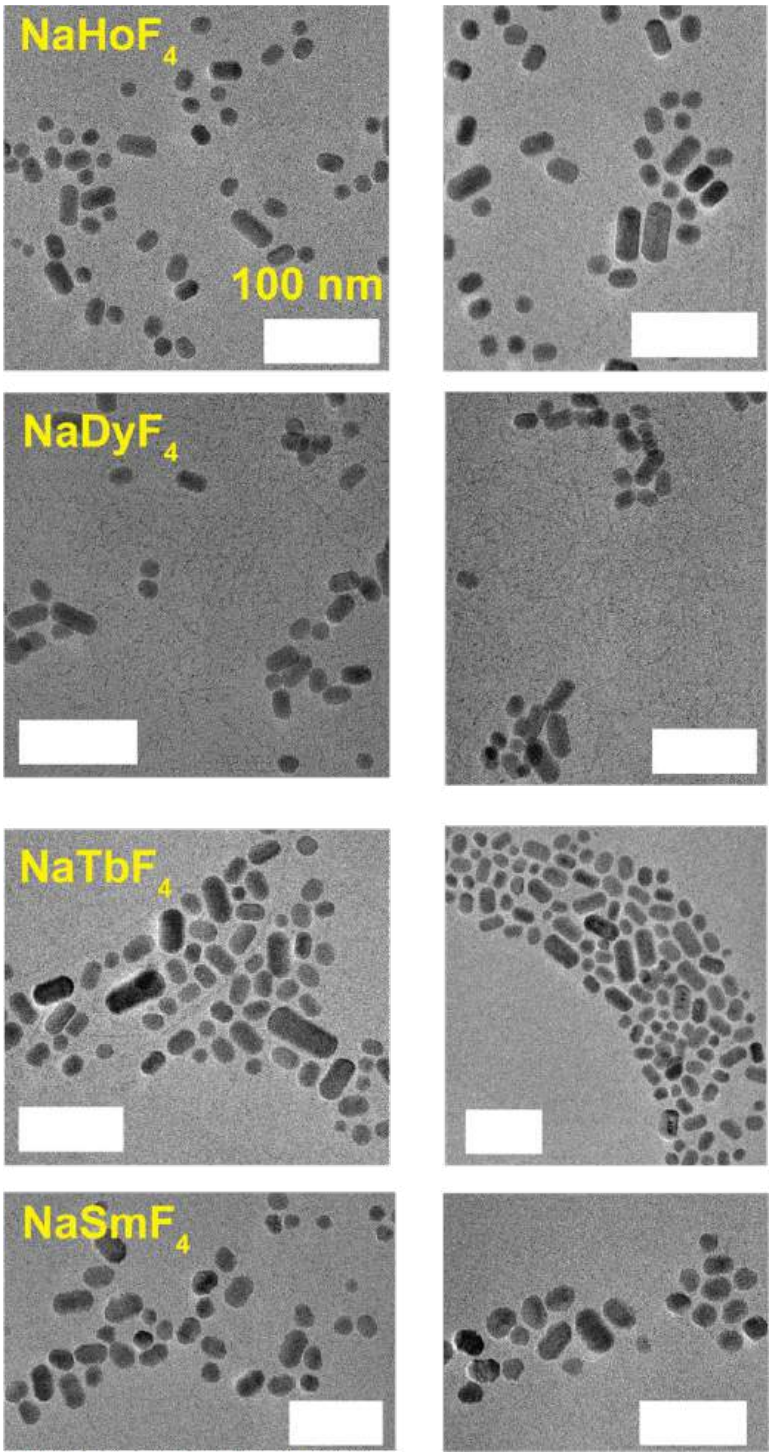

Supplementary Figure 2: TEM imaging of LNPs with 60-min growth step. TEM characterization of $NaHoF_4$, $NaDyF_4$, $NaTbF_4$, and $NaSmF_4$ LNPs synthesized using a 60-min growth step. Images were acquired at 200 keV beam energy using a JEOL JEM-F200 S/TEM in TEM mode. Scale bars: 100 nm.

was placed under an argon atmosphere and the temperature was increased to 320 °C at a rate of 18–28 °C min^{-1} (**Supplementary Figure 1**). The reaction temperature was maintained for 60 min before cooling to <30 °C by removing the heating mantle. The entire volume of the reaction mixture was placed in a borosilicate glass scintillation vial. Nanocrystals were stored as-

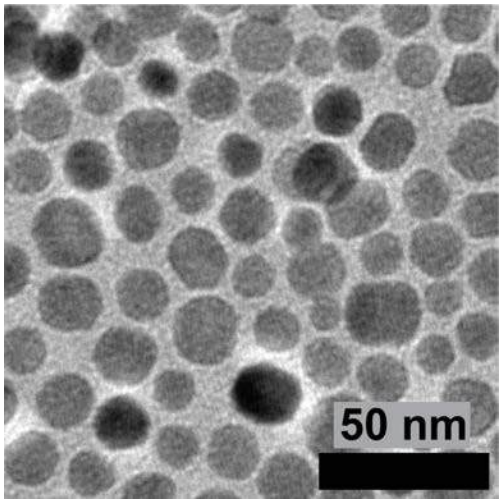

Supplementary Figure 3: TEM imaging of LNPs with 15-min growth step. TEM image of $NaHoF_4$ LNPs synthesized using a 15-min growth step. Images were acquired at 200 keV beam energy using a JEOL JEM-F200 S/TEM in TEM mode.

synthesized in oleic acid and 1-octadecene at room temperature. Representative TEM images of nanocrystals are shown in **Supplementary Figure 2**.

For smaller $NaHoF_4$ nanocrystals, the synthesis was performed as described above, except that the 320 °C reaction temperature was maintained for 15 min, not 60 min, before cooling to <30 °C (**Supplementary Figure 3**). For smaller, uniformly shaped $NaHo_{0.8}Lu_{0.2}F_4$ nanocrystals, the synthesis was performed as described above, except that the 0.5 mmol of lanthanide chloride hydrates was divided into two quantities based on the desired molar ratio of the two lanthanide elements, and the 320 °C reaction temperature was maintained for 2.5 min, not 60 min, before cooling to <30 °C (**Supplementary Figure 4**).

Supplementary Note 2. Nanoparticle sample preparation

For nonlocal CL excitation experiments involving a dense nanocrystal region and a sparse nanocrystal region separated by a well-defined edge, the samples were prepared as follows: 0.5 mL of as-synthesized nanocrystals was washed by mixing with 0.5 mL of ethanol and centrifuging at 3,500 × g for 3 min. The pellet was resuspended in 0.5 mL of n-hexane, mixed with 0.5 mL of ethanol, and centrifuged again; this step was repeated for a total of five

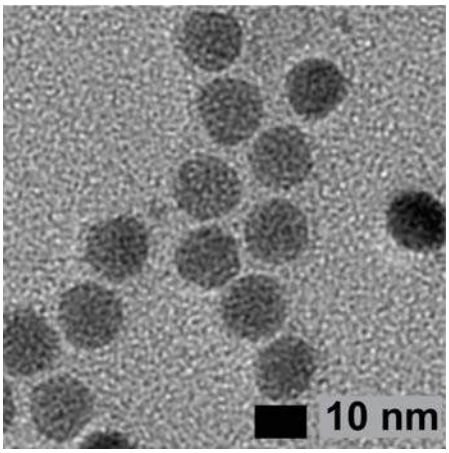

Supplementary Figure 4: TEM imaging of small, homogeneous LNPs. TEM image of $NaHo_{0.8}Lu_{0.2}F_4$ LNPs synthesized using a 2.5-min growth step. Images were acquired at 200 keV beam energy using a JEOL JEM-F200 S/TEM in TEM mode.

washes. After the fifth wash, the pellet was resuspended in 0.5 mL of n-hexane. A piece with a total area of ≈1 cm^2 was cut from a p-type Si wafer (Ted Pella, Cat# 16015), cleaned with 70% ethanol, and plasma cleaned. Then, half of its surface was covered with tape (Scotch Magic Tape). 5 µL of the desired n-hexane-suspended nanocrystals was drop-cast onto the exposed half of the Si wafer's surface. After the n-hexane dried, drop-casting was repeated four times to create a thick layer of dense nanocrystals. Finally, the tape was removed from the Si wafer's surface, the desired n-hexane-suspended single nanocrystals (preparation described below) were diluted 100–1,000× in n-hexane to achieve sparsity, and 5 µL was drop-cast onto the wafer.

For experiments requiring samples of single nanocrystals with minimal aggregation, 0.5 mL of as-synthesized nanocrystals was washed by mixing with 5 mL of ethanol and centrifuging at 5,000 × g for 10 min. The pellet was resuspended in 1 mL of n-hexane, mixed with 5 mL of ethanol, and centrifuged again; this step was repeated for a total of five washes. After the fifth wash, the pellet was resuspended in 5 mL of n-hexane and the solution was left undisturbed overnight. For further sample preparation, nanocrystals were pipetted from the top of the solution to avoid collecting precipitated nanocrystal aggregates. For characterization by TEM, 2 µL of the nanocrystal solution was drop-cast onto a copper TEM grid (Ted Pella, Cat# 01810); for characterization by SEM, 5 µL of the nanocrystal solution was drop-cast onto an ethanol- and plasma-cleaned p-type Si wafer (total area ≈1 cm^2).

Supplementary Note 3. Impact of dopant concentration on LNP brightness

To investigate the impact of dopant concentration on the brightness of LNPs, we synthesized co-doped LNPs containing Dy^{3+} and Y^{3+} ions. Y^{3+} ions were chosen as spectator ions because unlike lanthanide ions, their f-orbitals are empty. Y^{3+} ions are known to reduce non-radiative energy losses that arise due to interactions between proximal lanthanide ions[4]. Such co-doping with Y^{3+} is also commonly used to study the impact of concentration quenching in optically addressable upconverting LNPs[5]. We found that the brightness of the LNPs increased with higher Dy^{3+} concentrations, reaching a plateau at approximately 20% (**Supplementary Figure 5**). This plateau likely resulted from concentration quenching, where the increased brightness from additional emitting centers, i.e., lanthanide ions, was offset by increased interactions between lanthanide ions at higher concentrations.

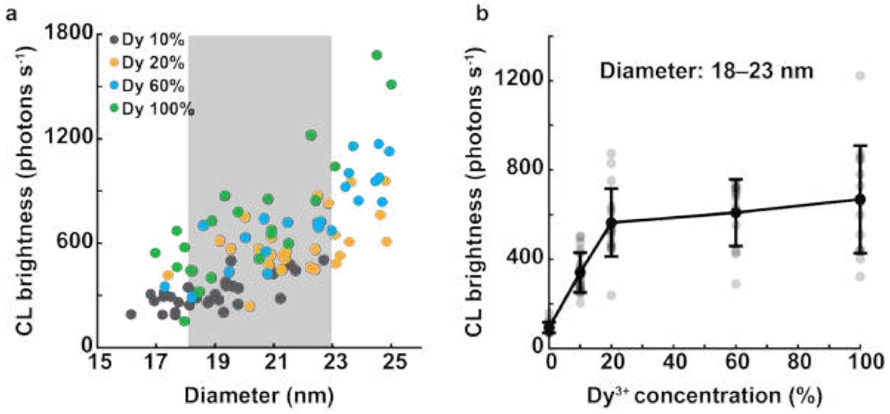

Supplementary Figure 5: CL brightness and dopant concentration. (a) Brightness of LNPs in the Dy^{3+} channel as a function of size for different dopant concentrations. At least 25 LNPs were imaged for each condition. **(b)** Brightness of LNPs of sizes between 18 and 23 nm as indicated by the shaded region in (a). Brightness is plotted as a function of dopant concentration. Different dopant concentrations were achieved by mixing Dy^{3+} ions with Y^{3+} ions, except for 0% Dy^{3+}, which shows emission of $NaGdF_4$ ions in the Dy^{3+} channel. Error bars in (b) show mean and standard deviation of 18, 20, 17, 12, and 14 LNPs, for dopant concentrations of 0%, 10%, 20%, 60%, and 100% respectively. Source data are provided as a Source Data file.

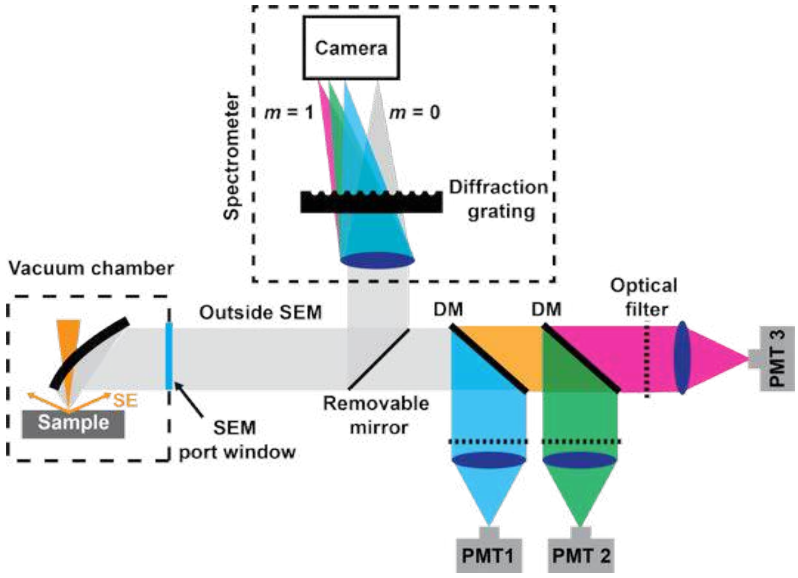

Supplementary Figure 6: Schematic of the CL detection system. A parabolic mirror was installed inside the vacuum chamber of the SEM to collect light from the sample. The mirror had a 500-µm-diameter aperture through which the electron beam passed to reach the sample. The mirror directed light outside the vacuum chamber, where a system of dichroic mirrors (DMs), optical filters, and lenses was used to focus it onto PMTs. Three PMTs were used to simultaneously collect light over three spectral ranges. To collect spectra, a removable mirror was inserted in the emission path to direct light towards the spectrometer consisting of a diffraction grating and an sCMOS camera. *m* is the diffraction order of the grating.

Supplementary Note 4. CL detection system

CL was collected by a parabolic mirror installed inside the vacuum chamber of a ZEISS SUPRA 55VP SEM. See **Supplementary Figure 6** for a schematic of the setup. The mirror was installed on a five-axis nanopositioning stage system (Attocube) to precisely align the center of the field-of-view (FOV) of the SEM to the focal point of the mirror. The mirror was custom-manufactured by diamond turning (B-con Engineering). The mirror had a focal length of 1 mm and collected CL over an average solid angle of ≈1.34π steradians. The mirror collimated light from the sample and directed it outside the vacuum chamber through an anti-reflection-coated fused silica flat window (Thorlabs, VPW42-A) installed on the custom-modified side port of the SEM. The light was then spectrally separated using dichroic mirrors, filtered using band-pass filters matched to the emission peaks of LNPs (**Supplementary Figure 7**), and focused onto PMTs (Hamamatsu, H7421-40) using 30-mm-focal-length tube lenses (Thorlabs, AC254-030-A-ML).

Custom spectrometer: For spectral measurements, a fold mirror was inserted in the emission path to redirect the CL towards the spectrometer. The light was focused onto an sCMOS camera (Hamamatsu, Orca-Fusion BT) using a 100-mm-focal-length lens (Thorlabs, AC254-100-A-ML). A diffraction grating (Thorlabs, GT13-03) was placed in front of the sCMOS camera to spectrally separate the CL signal.

Commercial spectrometer for ensemble measurements: The spectra of the ensemble of nanocrystals were measured using a commercial spectrometer (Thorlabs, CCS200). Collimated light from the parabolic mirror was focused on the multimode fiber of the spectrometer. The accompanying software was used to obtain the spectra. Ensemble spectra were obtained by scanning a 400 nm x 400 nm region of dense LNPs with a beam energy of 3 keV. Note that the ensemble spectra presented in **Fig. 1a** and **Supplementary Figure 7** were

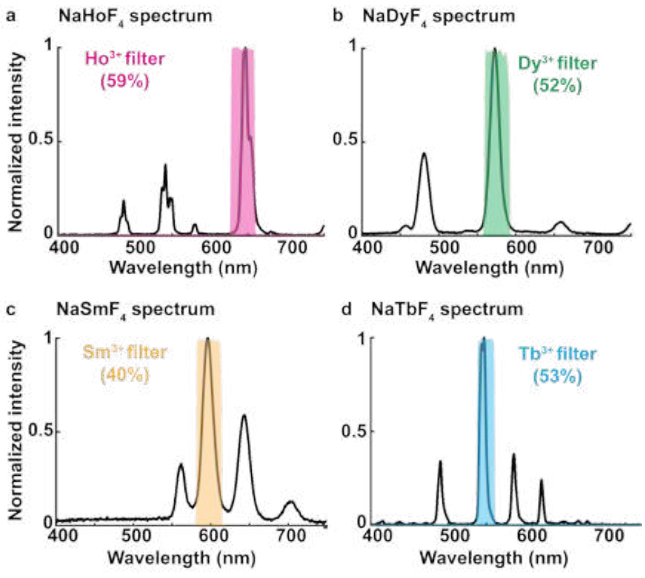

e Transmission of cathodophores across different filters

Filter	Details	$NaHoF_4$ transmission	$NaDyF_4$ transmission	$NaSmF_4$ transmission	$NaTbF_4$ transmission
Ho^{3+} filter	Chroma ET645/30X	59%	3%	24%	1%
Dy^{3+} filter	Chroma FF03-575/25	3%	52%	18%	14%
Sm^{3+} filter	Semrock FF01-598/25	1.2%	7%	40%	15%
Tb^{3+} filter	Chroma ET550/20X	14%	2%	4%	53%

Supplementary Figure 7: CL emission spectra and spectral filters. (a–d) CL emission spectra of $NaHoF_4$, $NaDyF_4$, $NaSmF_4$, and $NaTbF_4$ LNPs, respectively. Spectra were obtained from an ensemble of LNPs. Shaded bands in each subpanel show transmission profiles of the band-pass emission filters matched to the emission peaks of the respective dopants. **(e)** Information about the band-pass emission filters. CL transmission efficiency for each dopant across the filters is also shown. Source data are provided as a Source Data file.

obtained using the commercial spectrometer. All the other spectra presented in this work were obtained using the custom spectrometer.

Supplementary Note 5. Image acquisition

LNP characterization: Images were acquired using custom software written in LabVIEW. The software communicated with the hardware (SEM and the PMTs) through an NI DAQ card (National Instruments, PXIe-6368). Scanning of the electron beam, collection of CL signal on three PMTs, and collection of electron signal on the Everhart-Thornley detector of the SEM (SE channel) were synchronized. We navigated the sample using the ZEISS SmartSEM software. Once a region of interest was identified, we switched to the “External Scan” setting of the SEM. In this setting, the electron beam scanning was controlled by the LabVIEW software. For each FOV, the oversampled SEM image from SmartSEM was saved, which was later used to determine the size of LNPs. Furthermore, during each scan of the FOV with the “External Scan” setting, four images were acquired: one SE image and three CL images (in different spectral channels).

For the characterization of emission properties of LNPs (**Fig. 4, Fig. 5c**), CL images were acquired with a single LNP per image. We scanned a small region, 20 × 20 pixels, around the LNP with a pixel size of 4–6 nm, meeting the Nyquist criterion for the smallest LNPs. Such an image acquisition pipeline, i.e., scanning a small region around nanocrystals, was important

to reduce overall imaging times because the effective dwell times in CL imaging were ≈3 orders of magnitude slower than typical SEM imaging. In summary, for each FOV two types of images were acquired:

1. An oversampled SE image using the ZEISS Smart SEM software at regular scan speeds of the SEM (dwell time: 1–3 µs). This image was used to determine the size of LNPs.
2. A Nyquist-sampled SE and three CL images of the same FOV with longer dwell times. These images were used to characterize the emission properties of LNPs.

Multicolor imaging: Images were acquired using the setup described in **Supplementary Figure 6**. Multiple images were taken at a shorter dwell time to minimize charging related effects. An increase in charging was noted for denser samples used in multicolor experiments, which may be attributed to a higher concentration of organic solvents left behind after LNP washing. To accommodate this variability, we varied the beam dwell time between 100 µs and 1 ms, based on the extent of charging. Images were acquired with an effective beam dwell time of 30–50 ms per pixel. Drift correction was performed post-image acquisition.

Supplementary Note 6. Impact of field of view on nonlocal CL signal

The experiments discussed in **Fig. 2** were performed with a tube lens of 30 mm focal length, which resulted in a FOV >300 µm (>150 µm radius) as shown in **Supplementary Figure 8a**. Hence, CL signal from the sample region within 150 µm of the excited LNP was collected by the PMTs. We also reduced the FOV of the imaging system to confirm that the nonlocal CL signal was in fact originating from the sample, and was being collected by the parabolic mirror. To this end, we modified the FOV to ≈25 µm radius by changing the focal length of the tube lens to 400 mm (**Supplementary Figure 8a**). When we repeated the experiment with dense $NaDyF_4$ and sparse $NaHoF_4$ LNPs, the nonlocal signal in the Dy^{3+} color channel disappeared when $NaHoF_4$ LNPs were imaged at a distance >20 µm away from the edge (**Supplementary Figure 8b**). However, signal in the Ho^{3+} color channel was independent of the distance from the edge, which was expected if this signal originated from the excited LNP placed at the center of the FOV (**Supplementary Figure 8c**).

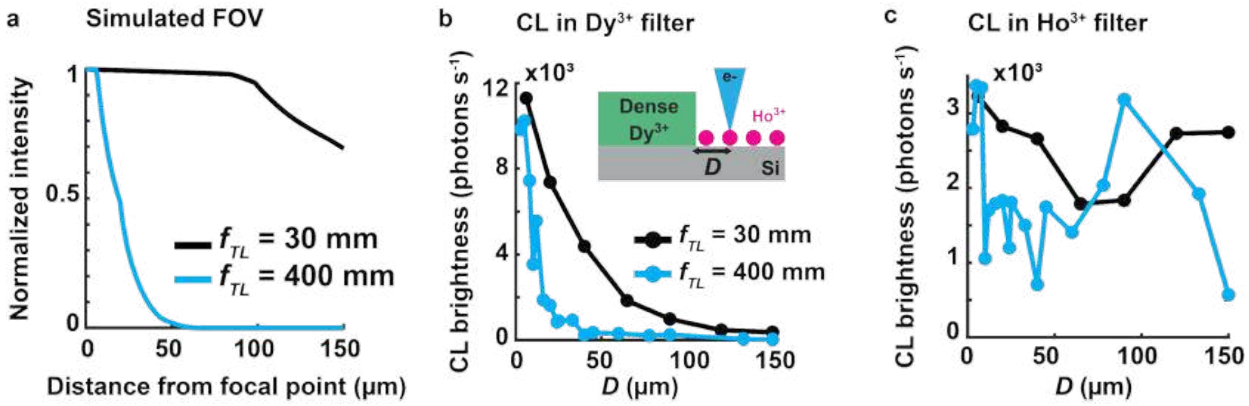

Supplementary Figure 8: Nonlocal excitation and field of view (FOV) of the parabolic mirror. (a) Simulation of light captured from a point source on a PMT of 5 mm diameter (matched to the PMTs used in this work). The point source was imaged at different distances from the focal point of the parabolic mirror for two different focal lengths of the tube lens (lenses placed in front of the PMTs in **Supplementary Figure 6**). The intensity was obtained by ray tracing and served as a measure of the FOV of the CL imaging system. The FOV had >150 µm radius for the 30 mm focal length tube lens, which was reduced to ≈25 µm for the 400 mm focal length tube lens. **(b,c)** Edge experiment with dense $NaDyF_4$ and sparse $NaHoF_4$ LNPs. Sparse $NaHoF_4$ LNPs were imaged at different distances from the dense region's edge. CL in Dy^{3+} and Ho^{3+} color channels are shown in (b) and (c), respectively. Source data are provided as a Source Data file.

Supplementary Note 7. Impact of atomic number on nonlocal CL signal

A counterintuitive aspect of the nonlocal CL signal was its dependence on the atomic number of the elements involved. For instance, the LNPs generated more stray electrons compared to the surrounding Si substrate. Consequently, at different distances from the thick LNP layer, the nonlocal signal originating from single LNPs was higher than that of the substrate, making the signal appear to originate from the LNPs (**Fig. 2b**).

This behavior is illustrated using Monte Carlo simulations in **Supplementary Figure 9b**, where the energy absorbed by a 10-µm-high layer is plotted for LNP and Si substrate excitation at varying distances. At every point, the nonlocal signal contributed by the LNP was consistently higher than that of the Si substrate. **Supplementary Figure 9c** shows simulated images of a $NaHoF_4$ LNP on the Si substrate in the Dy^{3+} channel at two different distances, 1 µm and 100 µm, from the layer. These images were generated by determining the energy absorbed by the layer at each pixel of the image. The signal corresponded to the Dy^{3+} channel because the layer was composed of $NaDyF_4$ LNPs. At 1 µm away from the layer, the nonlocal signal from both the Si substrate and the LNPs was higher compared to the signal at 100 µm. However, in both cases, the LNP exhibited a stronger signal because it produced more stray electrons than Si.

Supplementary Figure 9d–f shows the experimental results for the schematic shown in **Supplementary Figure 9a**, where sparse $NaHoF_4$ LNPs were imaged at different distances from the dense $NaDyF_4$ layer. Similar to the simulation results, we observed nonlocal signal from both

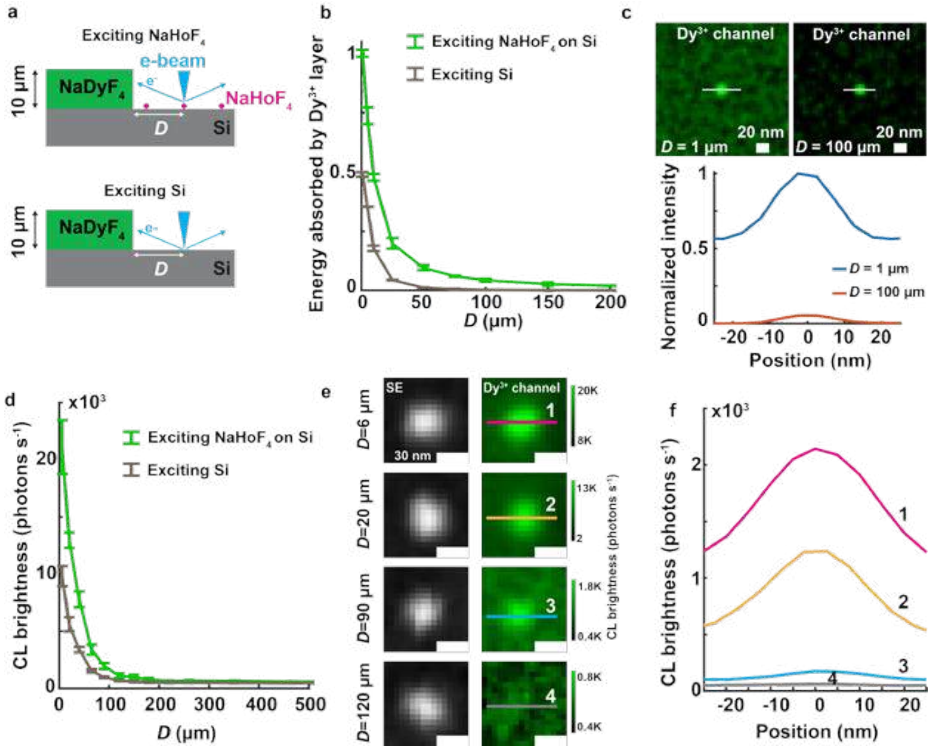

Supplementary Figure 9: Nonlocal excitation from Si vs. LNPs. (a) Illustration of the two sample configurations used to perform Monte Carlo simulations. **(b)** Monte Carlo simulation of the energy absorbed by a thick $NaDyF_4$ layer upon excitation of a 20 nm $NaHoF_4$ LNP and Si at different distances. Three data points were simulated at each *D*. **(c)** Simulated images (top row) of a $NaHoF_4$ LNP on the Si substrate in the Dy^{3+} channel at distances (*D*) 1 µm and 100 µm from the $NaDyF_4$ layer. The images were generated by determining the energy absorbed by the layer at each pixel of the image. Cross-sectional profiles of simulated images (bottom row). **(d)** Experimental CL emission in the Dy^{3+} channel from $NaHoF_4$ and Si at different distances from the dense $NaDyF_4$ layer. Five LNPs were imaged at each *D*. **(e)** SE and CL images of LNPs at different distances from the dense layer, from the experiment shown in (d). **(f)** Cross-sectional profiles of the LNPs shown in (e). In (b,d) error bars show mean and standard deviation of the data. Source data are provided as a Source Data file.

the Si substrate and $NaHoF_4$ LNPs in the Dy^{3+} channel, and this signal decreased as a function of distance from the dense layer of $NaDyF_4$ LNPs. However, at any distance, the nonlocal signal from the LNPs was higher than the Si substrate because LNPs produced more stray electrons. Consequently, the local increase in CL signal at a LNP's position made it difficult to categorize the signal as nonlocal, and therefore to distinguish it from the true CL signal emitted by the LNP being imaged.

Supplementary Note 8. Can X-rays cause nonlocal CL?

We further investigated the origin of the nonlocal CL signal, with the goal of determining whether it could be caused by X-rays originating from the excited LNPs, instead of stray electrons.

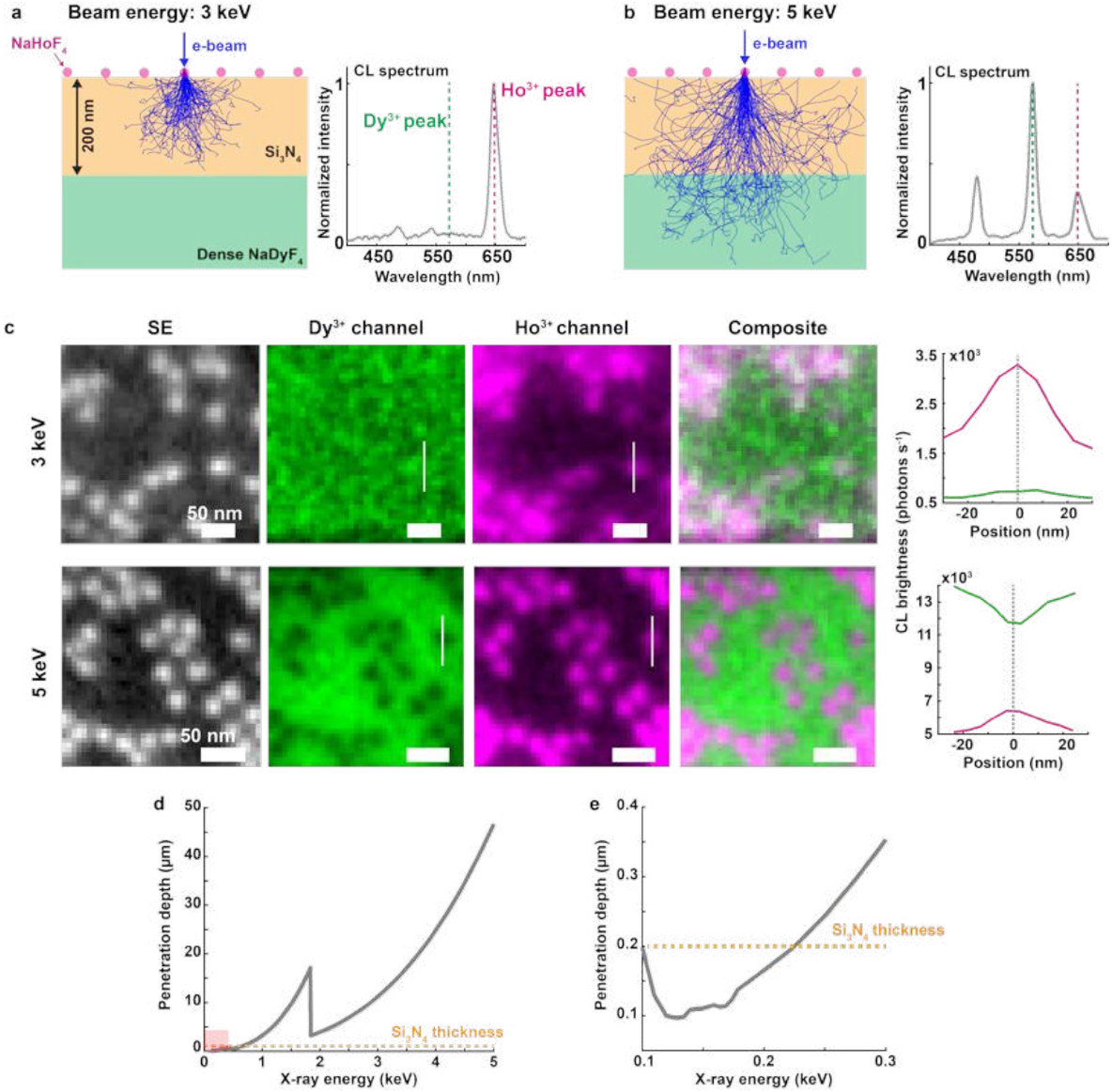

Supplementary Figure 10: Photonic emission from LNPs does not cause nonlocal excitation. **(a,b)** Monte Carlo simulations and measured CL spectra of the sample where sparse ($NaHoF_4$) and dense ($NaDyF_4$) LNPs were separated by a 200-nm-thick layer of Si_3N_4 coated with a 5-nm-thick layer of 80:20 Pt:Pd on its top surface (not shown). **(c)** Left: SE and CL images acquired from the sample shown in (a,b), at beam energies of 3 keV and 5 keV. Right: Cross-sectional profiles corresponding to the white lines shown in CL images (left). Profiles are shown for both Dy^{3+} (green) and Ho^{3+} (magenta) channels. **(d)** Penetration depth of X-rays inside Si_3N_4 as a function of X-ray energy. **(e)** Zoom-in of the graph from the shaded region in (d) over 0.1 to 0.3 keV. Dotted lines in (d,e) highlight the thickness of Si_3Ni_4 used. Source data are provided as a Source Data file.

To test this hypothesis, we used the system shown in **Supplementary Figure 10**, where a 200-nm-thick Si_3N_4 window (Ted Pella, Cat# 21522-10) was used to separate dense and sparse LNPs. The top surface was coated with a 5-nm-thick layer of 80:20 Pt:Pd to reduce charging artifacts. Dense $NaDyF_4$ LNPs were added on one side of the window and sparse $NaHoF_4$ on the other. $NaHoF_4$ LNPs were imaged with electron beam energies of 3 keV and 5 keV. CASINO simulations of the setup along with the measured CL spectra are shown in **Supplementary Figure 10a,b**. At 3 keV, the electron penetration depth was less than 200 nm and the $NaDyF_4$ LNPs were not excited. Consequently, the detected CL spectrum only contained the peak corresponding to Ho^{3+} ions. Conversely, at 5 keV, the electron penetration depth was large enough to reach the $NaDyF_4$ LNPs, and both Ho^{3+} and Dy^{3+} peaks were observed in the CL spectrum.

Supplementary Figure 10c shows SE and CL images of $NaHoF_4$ LNPs. At 3 keV, no correlation was observed between the LNP location in the Ho^{3+} channel and signal in the Dy^{3+} channel. In fact, when the beam energy was increased to 5 keV, we observed a reduction in the signal in the Dy^{3+} channel at the locations of the Ho^{3+} LNPs. We attribute this signal reduction to the reduced interaction volume inside $NaDyF_4$ LNPs when $NaHoF_4$ LNPs were excited compared to Si_3N_4, i.e., we reason that $NaHoF_4$ LNPs were blocking the primary electron beam and preventing it from effectively reaching $NaDyF_4$ LNPs.

Compared to electrons, X-rays with energies greater than 250 eV could pass through the 200-nm-thick Si_3N_4 window (**Supplementary Figure 10d,e**), and the characteristic X-rays generated by elements in the LNPs were above 250 eV[6]. However, $NaDyF_4$ LNPs were only excited at 5 keV, when the electron beam energy was sufficient for electrons to pass through the Si_3N_4 window.

Sub-250 eV emission from LNPs, including soft X-rays and ultraviolet radiation, corresponding to electron binding energies at various energy levels within these elements[6], were blocked by the 200-nm-thick Si_3N_4 window. Such blocking of emission was different from the experimental conditions discussed in **Fig. 2** where no such substrate was present. However, we argue that these low-energy forms of radiation were less likely to produce a CL signal, given that high-energy X-rays did not. Nonetheless, we have not directly confirmed this hypothesis.

Overall, these results support the hypothesis that stray electrons are more likely to cause the nonlocal excitation of LNPs than X-rays or optical emission from $NaHoF_4$ LNPs. The penetration depth of X-rays within Si_3N_4 was obtained from the Center for X-Ray Optics, Lawrence Berkeley National Laboratory (LBNL)[7].

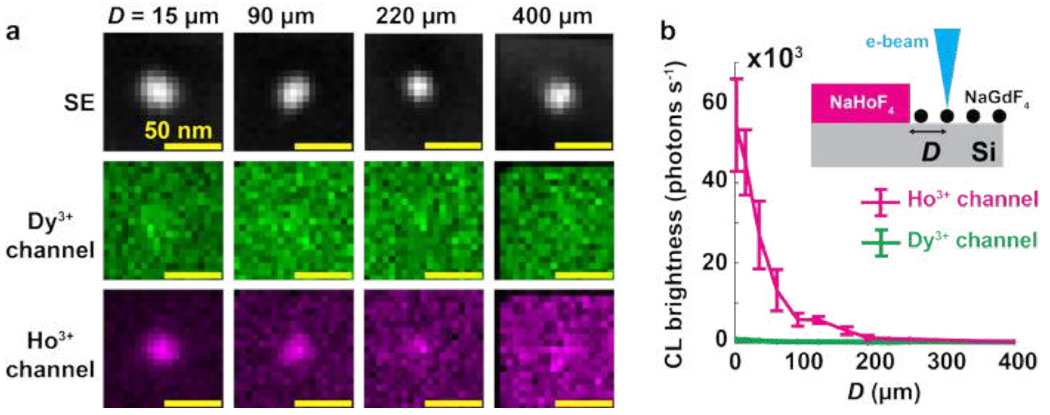

Supplementary Figure 11: Nonlocal excitation from LNPs with no emission peak in the visible range. (a) SE and CL images of $NaGdF_4$ LNPs at different distances from the edge of a dense $NaHoF_4$ LNP layer (>10 µm height). Due to nonlocal excitation of the $NaHoF_4$ LNP layer by stray electrons originating from $NaGdF_4$ LNPs, $NaGdF_4$ LNPs were visible in the Ho^{3+} color channel when they were imaged close to the layer's edge. **(b)** Rate of CL emission from $NaGdF_4$ LNPs at different distances from the edge. Four LNPs were imaged at each *D*. Error bars show mean and standard deviation of the data. Source data are provided as a Source Data file.

Supplementary Note 9. Nonlocal excitation when imaging different nanoparticles

To rule out the possibility that nonlocal CL excitation arises from non-radiative energy transfer (we already ruled out radiative energy transfer in Supplementary Note 8), we repeated the experiment shown in Fig. 2 of the main text using different sparse nanoparticles. Non-radiative energy transfer mechanisms such as FRET and Dexter transfer occur over short distances (<20 nm) and cannot account for the long-range (>100 μm) effects observed in our experiments[8,9]. Nonetheless, to thoroughly exclude such mechanisms, we used a dense layer of $NaHoF_4$ LNPs in combination with sparse nanoparticles (NPs) of different electronic structures, i.e., $NaGdF_4$, $NaYF_4$, and Au.

Supplementary Figure 11 shows the results of exciting sparse $NaGdF_4$ LNPs at different distances from a dense $NaHoF_4$ layer. As expected, we observed a signal in the Ho^{3+} emission channel when the $NaGdF_4$ LNPs were located near the edge of the $NaHoF_4$ layer. The signal decreased with increasing distance from the edge. The weak signal observed in the Dy^{3+} channel close to the layer was likely due to a minor spectral overlap between Ho^{3+} emission and the Dy^{3+} filter (3%, **Supplementary Figure 7**).

Although $NaGdF_4$ LNPs did not emit in the visible range, they contained the lanthanide ion Gd^{3+}. To determine whether the nonlocal signal depended on the presence of lanthanide ions, we

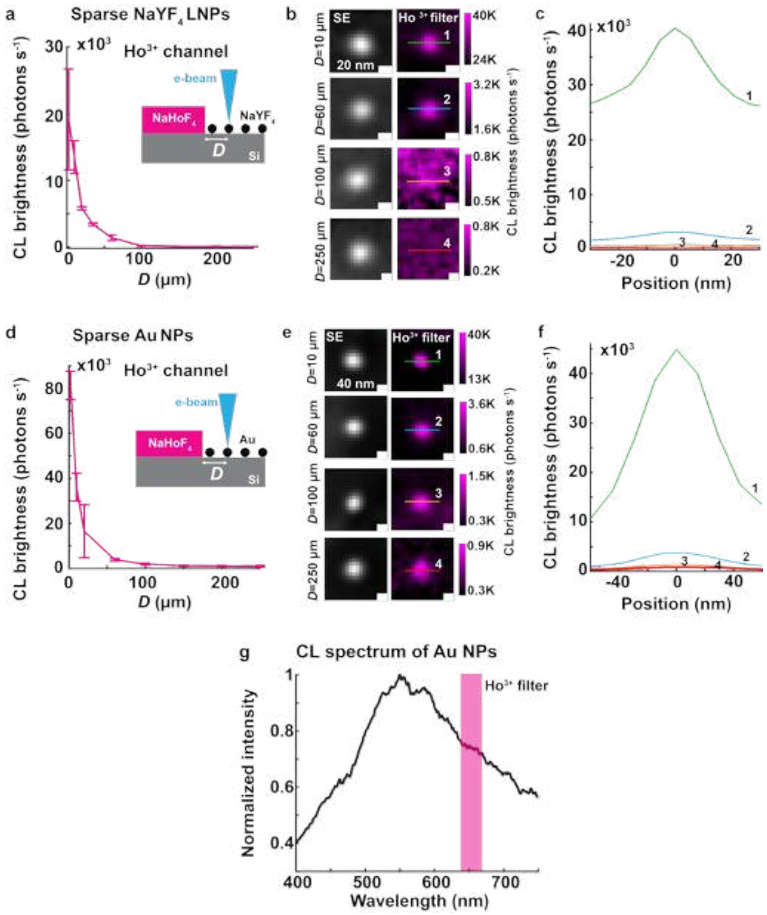

Supplementary Figure 12: Nonlocal excitation from non-lanthanide NPs. (a) CL signal in the Ho^{3+} channel from $NaYF_4$ NPs at different distances from the dense layer of $NaHoF_4$ LNPs. **(b)** CL images of $NaYF_4$ NPs at different distances from the layer. **(c)** Cross-sectional profiles of $NaYF_4$ NPs from (b). **(d)** CL signal in the Ho^{3+} channel from 40-nm-diameter Au NPs at different distances from the dense layer of $NaHoF_4$ LNPs. **(e)** CL images of Au NPs at different distances from the layer. **(f)** Cross-sectional profiles of Au NPs from (e). **(g)** CL spectra of Au NPs. Shaded band shows the transmission region of the Ho^{3+} filter. In (a,d) three LNPs were imaged at each *D*. Error bars show mean and standard deviation. Source data are provided as a Source Data file.

also tested non-lanthanide NPs, specifically $NaYF_4$ and Au NPs (Microspheres-Nanospheres, Cat# 790114-010, 40 nm), placed at different distances from the dense $NaHoF_4$ layer (**Supplementary Figure 12a,d)**. Under both conditions, we detected signal in the Ho^{3+} channel close to the dense layer, which decreased with distance from the layer. Moreover, the background signal from the Si substrate also reduced as a function of distance from the dense layer (**Supplementary Figure 12b,c,e,f**). This result indicates that the nonlocal signal was not an intrinsic property of lanthanide NPs and could be observed when exciting either the NPs or the substrate. However, it appeared to be localized at the spatial location of the NPs because they generated more stray electrons than the surrounding substrate.

The signal from $NaYF_4$ vanished at distances beyond 250 μm, whereas the Au NPs showed a location-independent signal at large distances from the dense layer. We attributed this distance-independent signal from Au NPs to their broadband plasmonic emission overlapping with the Ho^{3+} filter (**Supplementary Figure 12g**), consistent with previous reports[10,11].

These results demonstrated that the observed nonlocal signal did not depend on the specific type of NPs, whether lanthanide or non-lanthanide, further supporting the hypothesis that stray electrons are the source of nonlocal excitation.

Supplementary Note 10. Nonlocal CL signal on different substrates

After demonstrating that the nonlocal signal occurred for chemically distinct types of NPs, we tested whether it also existed for different substrates. This was done to rule out any charge carrier diffusion within the Si substrate that could potentially lead to nonlocal excitation.

First, we used Si_3N_4 as the substrate, consisting of a 200-nm-thick layer of Si_3N_4 on Si (Ted Pella, Cat# 21630-57). The experiment was performed using dense $NaHoF_4$ NPs and sparse

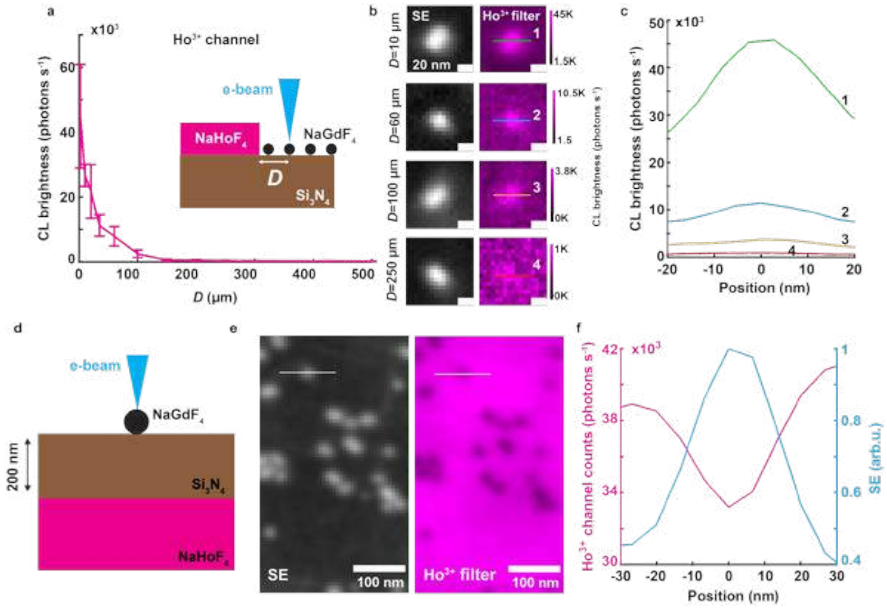

Supplementary Figure 13: Nonlocal excitation on Si_3N_4 substrate. (a) CL signal in the Ho^{3+} channel from $NaGdF_4$ LNPs on Si_3N_4 at different distances, *D*, from the dense layer of $NaHoF_4$ LNPs. **(b)** CL images of $NaGdF_4$ LNPs at different distances from the layer. **(c)** Cross-sectional profiles of LNPs from (b). **(d)** A schematic of imaging $NaGdF_4$ LNPs on a 200-nm-thick Si_3N_4 window coated with a 5-nm-thick layer of 80:20 Pt:Pd on its top surface (not shown). Dense $NaHoF_4$ LNPs were deposited on the opposite, lower side. A beam energy of 5 keV was used to penetrate through the Si_3N_4 layer and excite the $NaHoF_4$ LNPs (**Supplementary Figure 10**). **(e)** SE and CL images of the setup in (d). **(f)** Cross-sectional profiles of a particle marked in (e). In (a) three LNPs were imaged at each *D*. Error bars show mean and standard deviation. Source data are provided as a Source Data file.

$NaGdF_4$ NPs. As before, when imaging the sparse NPs, we observed a signal in the Ho^{3+} channel that decreased as a function of distance from the dense layer (**Supplementary Figure 13a–c**).

Moreover, to rule out energy transfer between NPs via the Si_3N_4 layer, we performed an additional experiment where $NaGdF_4$ NPs were placed directly on top of a 200-nm Si_3N_4 window (Ted Pella, Cat# 21522-10), and $NaHoF_4$ NPs were deposited on the opposite side (**Supplementary Figure 13d**). In this configuration, we observed a decrease in the signal at the location of the $NaGdF_4$ NPs rather than an enhancement, consistent with the results presented in **Supplementary Figure 10** (**Supplementary Figure 13e,f**). These experiments further supported the hypothesis that the nonlocal signal was caused by stray electrons and is independent of the substrate.

Next, we performed the experiment using an 80:20 Pt:Pd substrate, where a 200-nm-thick layer was sputter coated on Si. The dense NPs were $NaHoF_4$ and the sparse NPs were $NaGdF_4$. Again, a nonlocal signal was observed in the Ho^{3+} channel, which decreased with distance from the dense layer (**Supplementary Figure 14a–d**). In these experiments, we observed a high background signal from the substrate, likely due to its high atomic number, which resulted in the generation of many stray electrons. Since the diffusion lengths of charge carriers in metals are limited to a few tens of nanometers[12], the nonlocal CL signal was likely due to stray electrons.

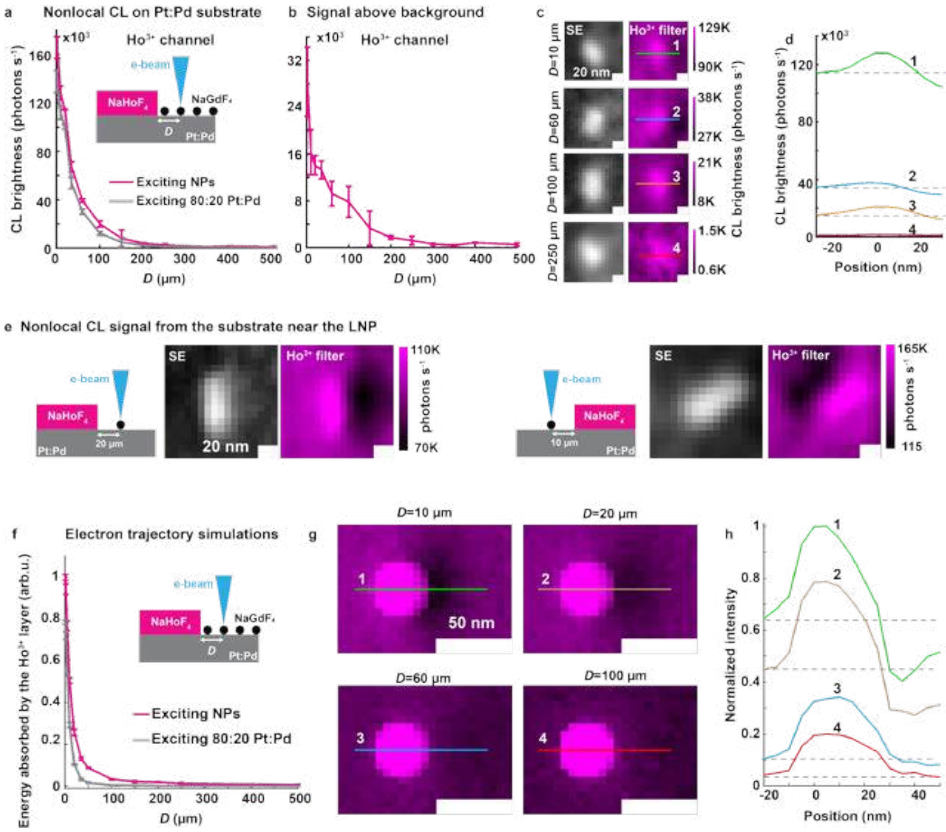

Supplementary Figure 14: Nonlocal excitation on Pt:Pd substrate. (a) CL signal from $NaGdF_4$ LNPs and the 80:20 Pt:Pd substrate at different distances from the dense layer of $NaHoF_4$ LNPs. Three LNPs were imaged at each *D*. **(b)** CL signal from the $NaGdF_4$ LNPs above the background (difference of the signals shown in (a)). **(c)** SE and CL images of $NaGdF_4$ LNPs at different distances from the layer. **(d)** Cross-sectional profiles of the LNPs from (c). **(e)** SE and CL images of LNPs imaged with different orientations of the dense layer. The shadows "behind" the LNPs were due to the LNPs blocking stray electrons from reaching the dense layer. **(f)** Simulation results of electron trajectory simulations (performed in CASINO software) of energy absorbed by the $NaGdF_4$ LNPs and 80:20 Pt:Pd substrate at different distances from the dense layer. Three data points were simulated at each *D*. **(g)** Simulated images of $NaGdF_4$ LNPs in the Ho^{3+} channel at different distances from the dense $NaHoF_4$ layer's edge. The images were generated by determining the energy absorbed by the layer at each pixel of the image. **(h)** Cross-sectional profiles of the LNPs from (g). Error bars show mean and standard deviation of the data. Source data are provided as a Source Data file.

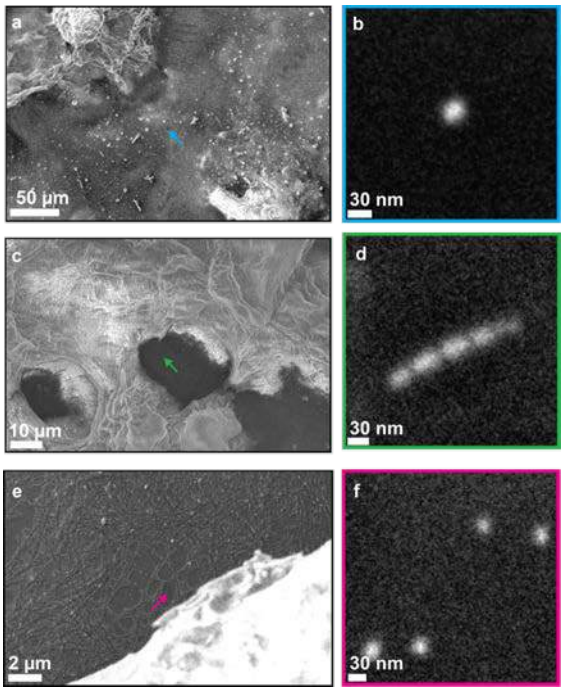

Supplementary Figure 15: Representative single LNP images in aggregated samples. (a,c,e) SEM images of samples containing aggregated and single $NaHoF_4$ LNPs. **(b,d,f)** Zoomed-in images of the regions marked with arrows in (a,c,e) showing imaging of single LNPs. When imaging single LNPs, the LNP aggregates were not imaged in the scanned region.

Interestingly, we observed a shadow in the CL signal of the substrate, always adjacent to a sparse NP and oriented such that the NP was between the shadow and the dense layer (i.e., the shadow was "behind" the NP) (**Supplementary Figure 14e**). We attributed this to the NPs blocking stray electrons, which originated from the substrate, from reaching the dense layer. This effect was more pronounced in the 80:20 Pt:Pd substrate due to their high atomic number compared to Si, and was also observed in our Monte Carlo simulations of electron trajectories (**Supplementary Figure 14f–h**).

Importantly, the Monte Carlo simulations only model electron trajectories and exclude radiative or non-radiative energy transfer mechanisms. The agreement between the simulations and experimental results, including the observed reduction in CL signal behind the NPs, indicates that stray electrons alone are sufficient to explain the nonlocal CL signal.

Supplementary Note 11. SEM imaging of single LNPs close to aggregates

For SEM imaging, we deposited LNPs on a Si substrate. If care was not taken to minimize LNP aggregation during sample preparation (see Supplementary Note 2), the substrate contained a mixture of LNP aggregates and single particles. In such cases, when imaging a single LNP, stray electrons generated from the excited particle could excite LNP aggregates located outside the scanned region but within the field of view of the parabolic mirror. **Supplementary Figure 15** shows three examples where LNP aggregates were present outside the scanned region at the high magnification needed to image single particles (**Supplementary Figure 15b,d,f**). These aggregates became visible only when we scanned the beam over a larger area by reducing the magnification of the SEM (**Supplementary Figure 15a,c,e**). The approximate locations of the scanned regions used to image single LNPs are indicated by arrows in the images.

Supplementary Note 12. Two-color and three-color imaging

Supplementary Figure 16 shows examples of two-color imaging in dense samples of $NaHoF_4$ and $NaDyF_4$ LNPs. **Supplementary Figure 17** shows the three-color image from **Fig. 3**, along with the three CL spectral channels. More examples of three-color CL images are shown in **Supplementary Figure 18.**

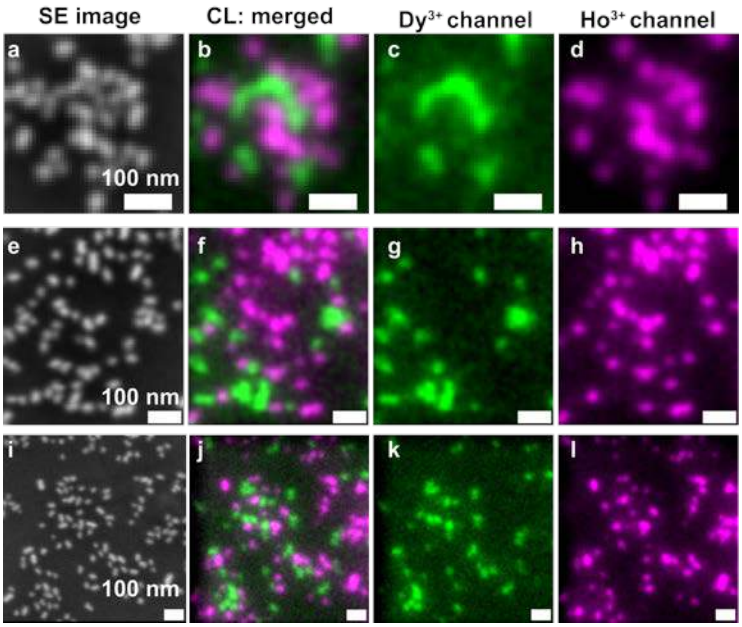

Supplementary Figure 16: Two-color CL imaging. (a,e,i) SE images of dense monolayers of samples containing $NaHoF_4$ and $NaDyF_4$ LNPs. **(b,f,j)** Corresponding CL images obtained by merging **(c,g,k)** Dy^{3+} and **(d,h,l)** Ho^{3+} color channels.

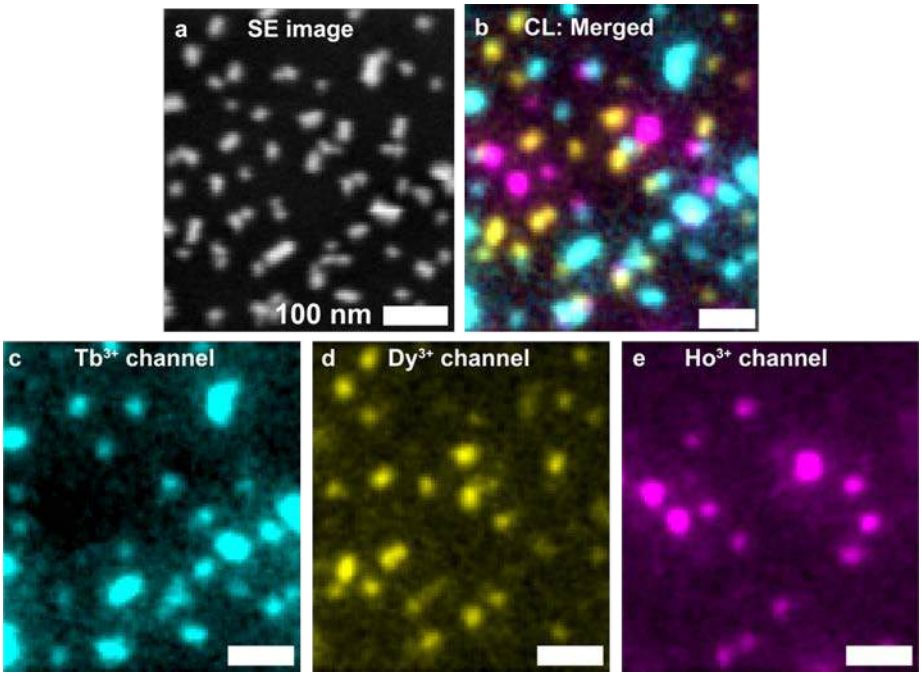

Supplementary Figure 17: Additional information on three-color imaging shown in Fig. 3k–n. (a) SE image of a dense monolayer containing $NaHoF_4$, $NaDyF_4$, and $NaTbF_4$ LNPs. **(b)** Corresponding CL image obtained by merging **(c)** Tb^{3+}, **(d)** Dy^{3+}, and **(e)** Ho^{3+} color channels. In (c) 15% of the intensity in the Ho^{3+} channel was subtracted from Tb^{3+} channel because minor peak of $NaHoF_4$ LNPs overlapped with the Tb^{3+} filter (**Supplementary Figure 7**). The factor was calculated from the ratio of the emission of $NaHoF_4$ LNPs in the Ho^{3+} and Tb^{3+} channels.

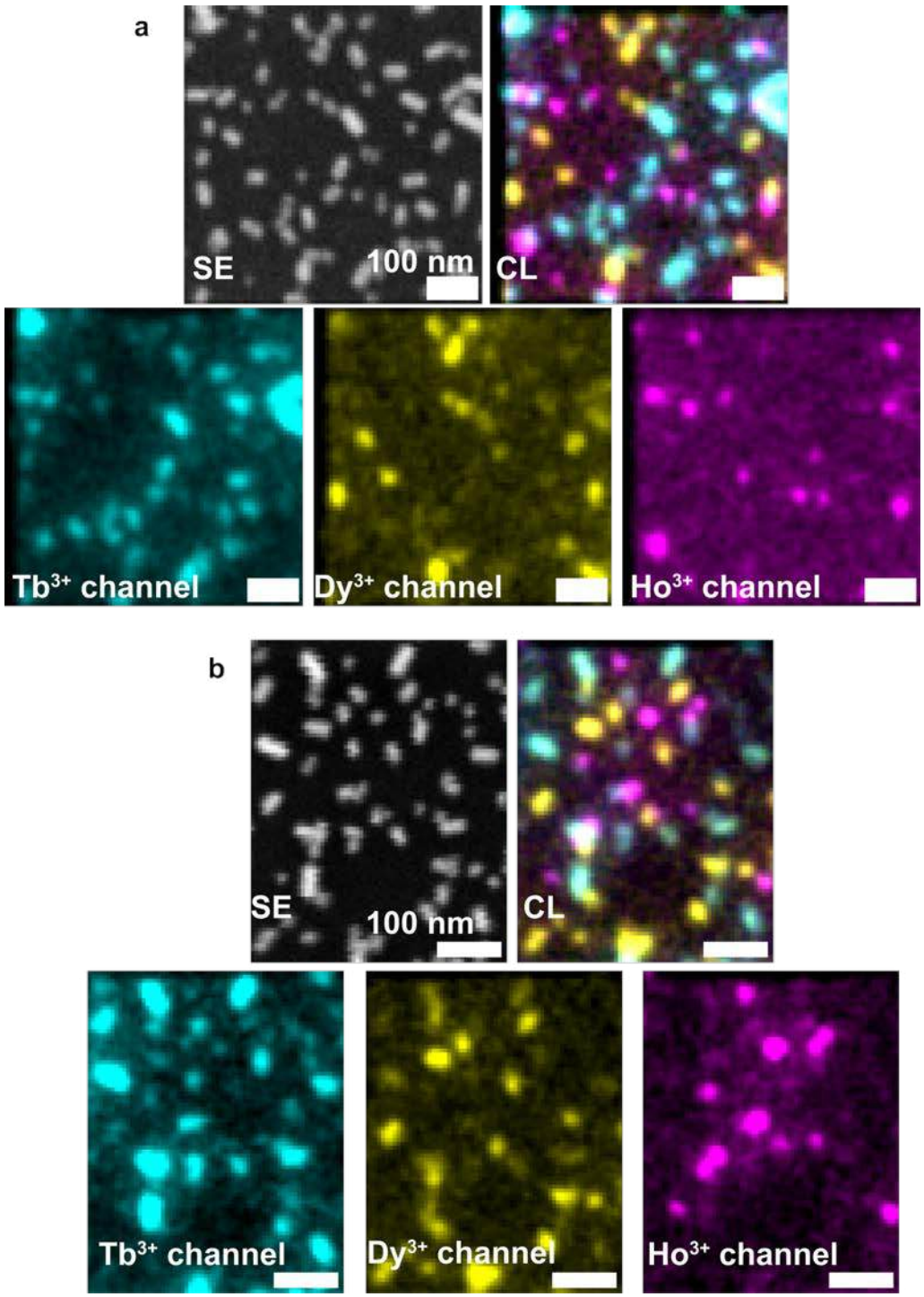

Supplementary Figure 18: Three-color CL imaging. More examples of CL imaging using $NaHoF_4$, $NaDyF_4$, and $NaTbF_4$ LNPs.

Supplementary Note 13. Automated dopant assignment in multicolor samples

Approach

We have developed a Bayesian classification framework for automatically assigning dopants to LNPs given the CL signals measured in Ho^{3+} and Dy^{3+} spectral channels (**Supplementary Figure 19**). We note that this classifier was developed as a proof-of-concept model for the exploratory analysis of the dataset presented here. While designed with future generalization in mind, further work will be required to validate its performance on more diverse datasets.

Model training

First, we trained our classification model using CL detection rates from single-LNP measurements. Specifically, we fitted a bivariate Gaussian distribution to the SE image of a LNP to obtain the LNP's position and size. We used these results as initial guesses in the following constrained optimization problem. Namely, in each CL channel separately, we used maximum likelihood estimation (MLE) to obtain the estimators of a bivariate Gaussian distribution modeling the LNP's CL signal. Noise was assumed to follow Poisson statistics. The CL detection rates were defined as the amplitudes of the obtained bivariate Gaussian distributions divided by the pixel dwell time.

We then compiled the detection rates from a set of single $NaHoF_4$ LNPs (N = 113) to model the relationship between the detection rate versus LNP diameter and beam dwell time in each spectral channel (as a quadratic surface). For a given dwell time and diameter, we further modeled the distribution of CL detection rates by a bivariate Gaussian distribution, whose location vector consisted of the expected detection rates (from the quadratic models), and whose covariance matrix reflected the variability in the rates in each channel. Due to the small size of the training set, the variance was computed over all LNPs (i.e., over all sizes) and the covariance between the channels was set to zero. As described below, we used the obtained distribution as a likelihood function to compute the probability that a LNP of a given diameter, at a given dwell time, was Ho^{3+}-doped. We repeated this analysis using a set of single $NaDyF_4$ LNPs (N = 65), to obtain a likelihood function for Dy^{3+}-doped LNPs.

Estimating CL detection rates in dense multi-LNP samples

The main challenge in dense multi-LNP samples was to minimize the bias that could be induced by neighboring LNPs on the photon measurements from the LNP of interest. To address this issue, we used LNP-specific masks. To this end, we started by modeling the ensemble of LNPs and the background in a multi-LNP SE image (e.g., **Supplementary Figure 19a**) to obtain a model of the image composed of an ensemble of bivariate Gaussian distributions on a quadratic surface (**Supplementary Figure 19b**). We then defined a LNP mask as the ensemble of pixels within 2σ of the distribution center (with σ the standard deviation of the Gaussian distribution) and that were not shared with any other LNP mask (**Supplementary Figure 19c**).

Equipped with these LNP-specific masks, we assessed the statistical significance and whether a local maximum could be detected for each LNP, in each spectral channel of the CL micrograph (**Supplementary Figure 19d**). Specifically, we attempted to run a chi-square goodness-of-fit test to compare the statistical significance of the CL pixel values under the LNP mask versus the CL pixel values in the local background near the LNP. If the test had at least 1 degree of freedom, it could be run and a P-value could be computed; however, if it had less than one degree of freedom, it could not be run, and the P-value could not be obtained. Note that for one LNP (#54), neither channel verified the test condition of minimum expected frequency of 5. For the completeness of the present analysis, the test was carefully extended to include this

LNP, by using a minimum frequency of 3. For all the other LNPs, classification results were identical whether the minimum frequency was 3 or 5. We also assessed whether a local maximum could be detected in the CL pixel values under the LNP mask by fitting linear and quadratic surfaces to them: if the adjusted R-squared of the fitted quadratic surface was the largest, and if both coefficients in the quadratic terms were negative, then we considered that a local maximum was detected.

For LNPs for which both P-values could be computed and local maxima were detected, we estimated the CL detection rates in each spectral channel (**Supplementary Figure 19e,f**). The analysis was similar to that performed to estimate the CL detection rates of single LNPs. Specifically, in each channel separately, we performed MLE assuming a Poisson noise, to obtain the estimators of a bivariate Gaussian distribution modeling the LNP's CL pixel values under the LNP mask and in the local background near the LNP. **Supplementary Figure 19e,f** illustrates how LNP-specific masks helped minimize the potential biases induced by neighboring LNPs on the estimation of the CL signal from the LNP of interest, even when the neighboring LNPs were bright. Finally, we performed dopant assignment using our probabilistic classification model, from the estimated CL detection rates in each spectral channel (**Supplementary Figure 19g,h**).

Dopant assignment

Probabilistic dopant assignment for LNPs whose CL detection rates could be measured in both spectral channels: We assigned a dopant to a LNP by computing the posterior probabilities that the LNP contained each possible dopant, given the detection rates in each spectral channel, and by selecting the dopant corresponding to the greatest of these probabilities. Specifically, we applied Bayes' theorem, using as prior probabilities the known fractions of each dopant in the sample (e.g., 50% for each Ho^{3+} and Dy^{3+} in **Supplementary Figure 19**); as likelihood functions, bivariate Gaussian distributions whose location vectors and covariance matrices were obtained during model training; evidence probability from the law of total probability; and as input evidence, the CL detection rates measured in each spectral channel.

Heuristic classification rules for LNPs whose CL detection rates could be measured at most in one spectral channel: We applied the following set of rules to assign—or not—a dopant to a LNP, based on whether, in each spectral channel, a P-value could be computed and a local maximum detected:

1. If no P-value could be computed in any channel: no dopant was assigned.
2. If a P-value could be computed in only one channel: the dopant was assigned corresponding to the channel of the only computed P-value.
3. If a P-value could be computed in both channels, and:
   a. If no local maximum was detected in either channel: the dopant corresponding to the channel with the smallest P-value was assigned.
   b. If a local maximum was detected in only one channel: the dopant corresponding to the channel with the local maximum was assigned.
   c. If local maxima were detected in both channels: probabilistic dopant assignment was performed.

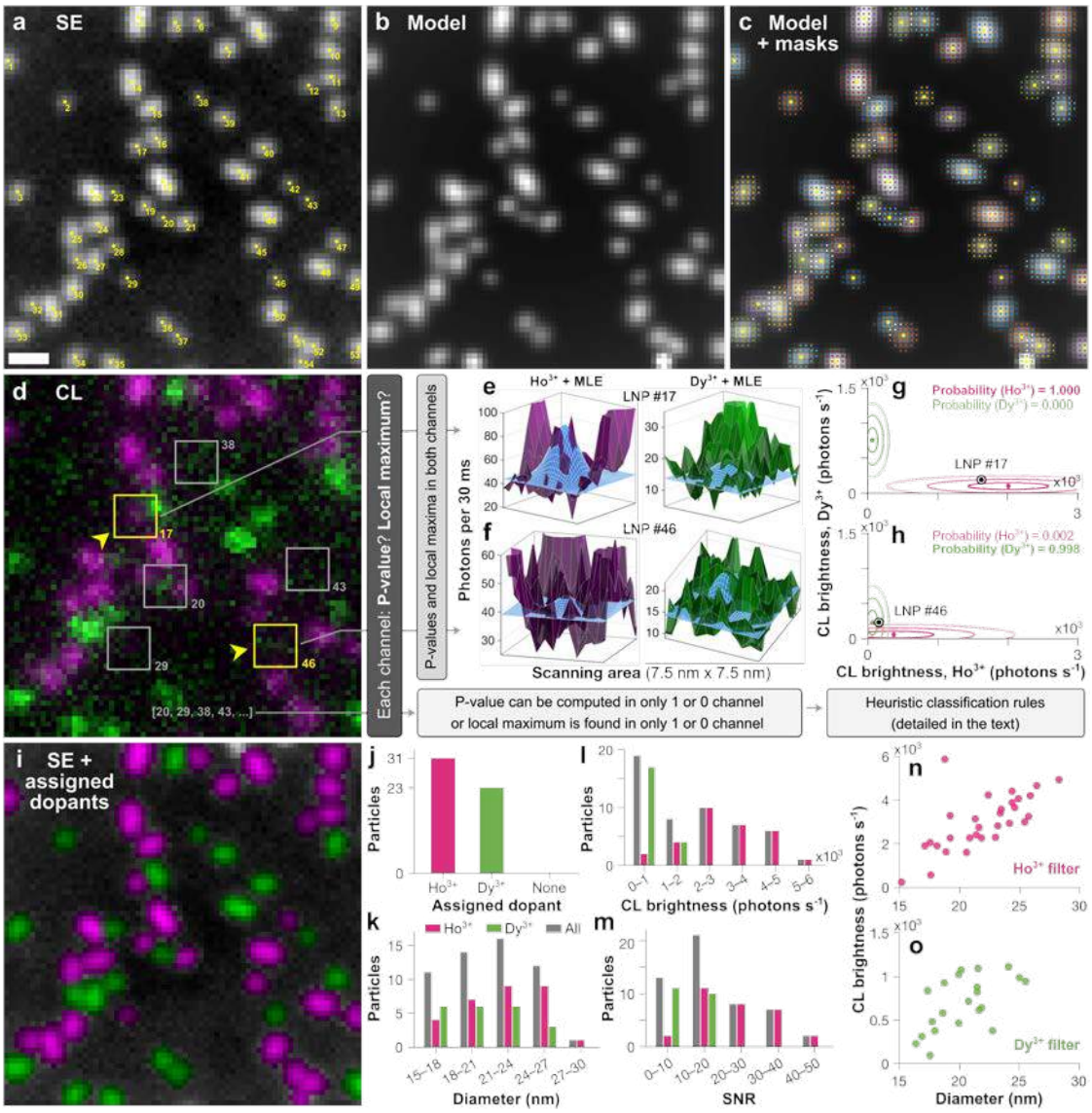

Supplementary Figure 19: Automated dopant assignment in multicolor samples. (a) SE image containing $NaHoF_4$ and $NaDyF_4$ LNPs (identical to **Fig. 3g**) with numerical identifiers overlaid. **(b)** Model for the SE image in (a), in which each LNP is represented as a bivariate Gaussian distribution and the background as a quadratic surface. **(c)** LNP-specific masks (small color dots) and centers (large yellow dots) obtained from, and overlaid on, (b). Pixels shared between two or more LNPs are excluded from all masks (white dots). **(d)** CL image showing overlaid Ho^{3+} and Dy^{3+} channels (identical to **Fig. 3h**). The yellow boxes highlight the two LNPs (#17 and #46) whose probabilistic dopant assignment analyses are detailed in (e–h). The yellow arrowheads indicate the viewing angles used in (e,f). Gray boxes show LNPs whose dopants were assigned by heuristic classification. **(e**,**f)** Estimation of CL detection rates. CL signal in the Ho^{3+} (left, magenta) and Dy^{3+} (right, green) channels for LNPs #17 (e) and #46 (f), and associated bivariate Gaussian distributions (blue) resulting from MLE of the CL signal under the LNP-specific masks. **(g,h)** Bayesian probabilistic dopant assignment. The estimated CL detection rates of LNPs #17 (g) and #46 (h) (bull's-eyes) are compared to our model trained on single-LNP datasets (ellipses and dots; magenta, $NaHoF_4$; green, $NaDyF_4$). The concentric ellipses represent the 1-σ, 2-σ, and 3-σ levels of the bivariate Gaussian distributions modeling the CL detection rates in the trained model. The color dots are the expected values. We assigned to each LNP the dopant with the greatest posterior probability. **(i)** SE image colorized according to assigned dopant (magenta, Ho^{3+}; green, Dy^{3+}). **(j–m)** Multicolor sample characterization (also see **Supplementary Table 1**). **(j)** Dopant assignment statistics. **(k)** Occurrences of LNP diameters. **(l,m)** Occurrences of estimated LNP CL detection rates (l) and occurrences of SNR (m) in the channel of the assigned dopant. **(n,o)** CL detection rates in the channel of the assigned dopant as a function of LNP diameter for Ho^{3+}-doped (n) and Dy^{3+}-doped (o) LNPs. (a–d, i) Contrast was adjusted. Scale bar: 50 nm. Source data are provided as a Source Data file.

LNP #	1	2	3	4	5	6	7	8	9	10	11	12	13	14	15
Assigned dopant	Ho^{3+}	Dy^{3+}	Dy^{3+}	Ho^{3+}	Dy^{3+}	Ho^{3+}	Ho^{3+}	Ho^{3+}	Ho^{3+}	Ho^{3+}	Ho^{3+}	Ho^{3+}	Dy^{3+}	Ho^{3+}	Ho^{3+}
Diameter (nm)	21.8	16.9	21.6	18.8	20.2	17.5	21.3	25.9	19.2	23.2	24.2	20.6	21.5	26.4	23.4
Photons s^{-1}	2265	314	615	5872	1075	2057	3143	4208	3287	2827	2935	1604	878	4667	3404
SNR	20	5	10	47	14	13	22	34	26	26	24	12	12	39	28

LNP #	16	17	18	19	20	21	22	23	24	25	26	27	28	29	30
Assigned dopant	Dy^{3+}	Ho^{3+}	Ho^{3+}	Ho^{3+}	Dy^{3+}	Ho^{3+}	Ho^{3+}	Dy^{3+}	Ho^{3+}	Ho^{3+}	Dy^{3+}	Dy^{3+}	Dy^{3+}	Ho^{3+}	Ho^{3+}
Diameter (nm)	25.0	18.9	28.3	20.8	18.0	23.0	24.9	22.8	24.4	25.7	20.0	25.5	20.8	15.2	22.4
Photons s^{-1}	986	1626	4943	2267	377	2293	4065	378	3888	3253	1026	945	716	238	4239
SNR	12	14	44	16	5	17	34	6	35	25	10	12	9	2	32

LNP #	31	32	33	34	35	36	37	38	39	40	41	42	43	44	45
Assigned dopant	Ho^{3+}	Ho^{3+}	Dy^{3+}	Dy^{3+}	Dy^{3+}	Dy^{3+}	Dy^{3+}	Dy^{3+}	Dy^{3+}	Dy^{3+}	Dy^{3+}	Ho^{3+}	Dy^{3+}	Ho^{3+}	Ho^{3+}
Diameter (nm)	24.6	18.1	21.6	18.7	17.4	17.7	20.0	16.8	21.9	21.5	24.1	17.6	17.6	24.4	17.1
Photons s^{-1}	3661	1905	1093	925	838	481	465	n/a	642	822	1112	564	95	4406	1905
SNR	30	13	14	12	8	6	6	n/a	10	11	17	6	1	37	15

LNP #	46	47	48	49	50	51	52	53	54
Assigned dopant	Dy^{3+}	Dy^{3+}	Ho^{3+}	Ho^{3+}	Ho^{3+}	Ho^{3+}	Ho^{3+}	Dy^{3+}	Ho^{3+}
Diameter (nm)	16.4	18.6	23.5	19.2	21.6	21.4	25.4	20.3	21.1
Photons s^{-1}	229	583	3582	2261	2752	2409	2996	n/a	n/a
SNR	3	8	31	17	25	19	19	n/a	n/a

Supplementary Table 1: Dopant assignment to the LNPs identified in **Supplementary Figure 19a** using our classification model, along with LNP diameter, and CL detection rate and SNR in the spectral channel of the assigned dopant. For LNPs #38, #53, and #54, dopant assignment was performed based on P-values and no local maximum was detected in the channel of the assigned dopant, thus photon rates and SNR could not be obtained.

Supplementary Note 14. Impact of nonlocal excitation on single-particle CL

The nonlocal excitation also impacted our single-color experiments. These experiments were an important first step to characterize the emission properties of LNPs prior to using them for multicolor imaging. In the presence of nonlocal excitation, the CL signal collected from an isolated LNP was independent of its size. This is because the signal was affected by the surroundings of the LNP, i.e., its distance from the luminescent aggregates that were excited by stray electrons (**Supplementary Figure 20a**). Once the nonlocal excitation was mitigated, we saw a linear dependence between the rate of CL detection from LNPs and their size (**Supplementary Figure 20b**), which is consistent with theoretical predictions (see **Supplementary Figure 28**).

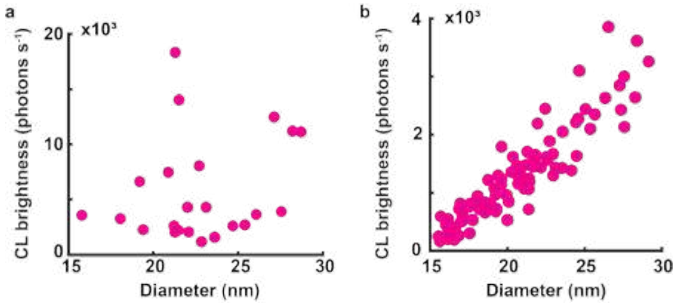

Supplementary Figure 20: CL signal vs. size in aggregated and non-aggregated samples. (a) CL brightness from single $NaHoF_4$ LNPs in a sample with aggregates of $NaHoF_4$ LNPs. CL collected from single LNPs was independent of their diameter (FWHM) due to nonlocal CL from the aggregates. **(b)** CL brightness from single $NaHoF_4$ LNPs in a sparse sample. The rate of detection depended linearly on the diameter of LNPs. CL was measured in the Ho^{3+} color channel. Source data are provided as a Source Data file.

Supplementary Note 15. Image analysis for single-particle characterization

Our image analysis involved:

- Drift correction
- Localization of the LNP in SE images
- Determination of the rate of CL detection and SNR from CL images
- Determination of the size of the LNP

Drift correction

Need for drift correction: A few hundred to a few thousand photons per second were collected from each LNP. Such a low rate of CL detection required imaging LNPs with a beam dwell time of tens of milliseconds to achieve the required SNR for detection and classification. Although LNPs were stable under the electron beam over multiple seconds, such a long beam dwell time led to a buildup of charge in the imaged region. As a result of this charging, the beam was deflected away from the imaged region, causing an apparent drift of the sample as shown in **Supplementary Figure 21**.

Drift correction during data acquisition: We typically acquired 50 frames, each with a pixel dwell time of 1 ms. During the acquisition of these frames, the LNP could drift out of the FOV. This problem was further exacerbated by the fact that we imaged a small FOV, 100 nm × 100 nm^2, with the LNP in the center. To ensure that the LNP remained in the FOV, we adjusted the center of the electron beam scan after each frame. To do this, we used the fact that LNPs, composed of heavy metals, were visible in the SE channel in each frame. Drift correction was performed by determining the position of the LNP in the FOV and adjusting the scan region accordingly. The LNP's position was determined as the location of the maximum intensity SE pixel in the FOV. This drift correction during data acquisition was only performed for LNP characterization experiments where a single LNP was imaged in a FOV. For all other experiments, i.e., multicolor imaging and those conducted to characterize the nonlocal CL signal, only post-acquisition drift correction was applied as described below.

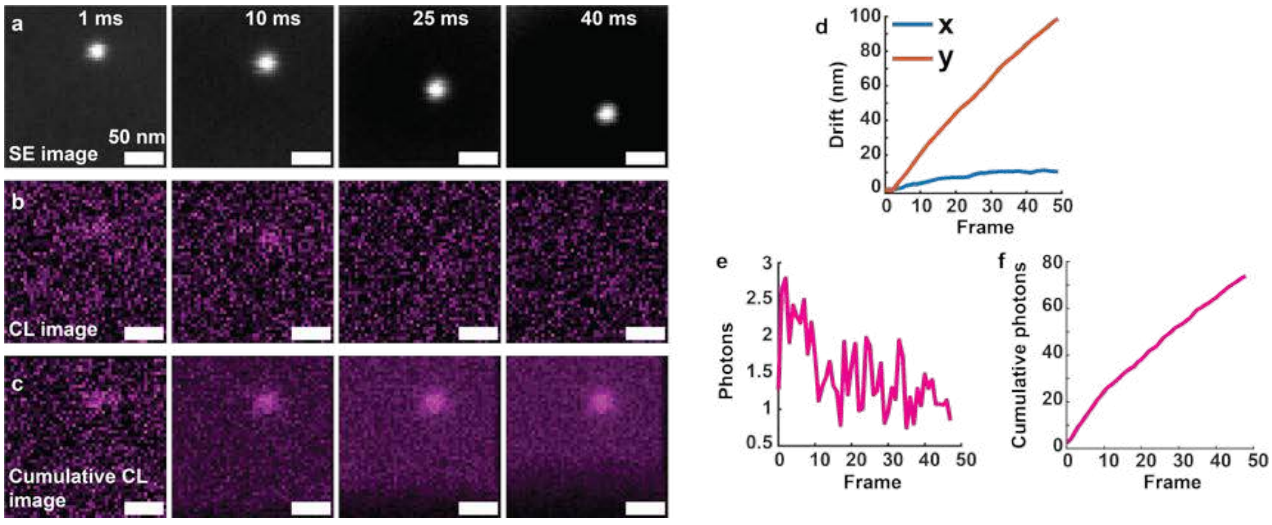

Supplementary Figure 21: Drift correction for CL imaging. (a) SE images of a LNP subjected to different total durations of electron beam exposure. The duration each pixel was exposed to the electron beam is shown in the top right corner of each image. Images were taken with a beam dwell time of 1 ms. **(b)** CL images acquired simultaneously with the SE images in (a). **(c)** Cumulative CL images obtained by summing the CL images from (b), to obtain the effective beam dwell times displayed in (a). Drift correction was applied prior to summing the images. **(d)** Displacement of the LNP relative to its position in the first frame. **(e)** Number of photons collected from the LNP as a function of the frame number. The number of photons corresponded to the amplitude of the 2D Gaussian fit to the CL images of the LNP as shown in (b). **(f)** Cumulative photons collected from the LNP, corresponding to the amplitude of the 2D Gaussian fit to the cumulative CL images of the LNP as shown in (c). Source data are provided as a Source Data file.

Post-acquisition drift correction: This drift correction was conducted after image acquisition. The position of the LNP was determined in all frames by fitting a 2D Gaussian function to each SE image frame. These positions were then used to translate the SE and CL frames to correct for the drift. The drift-corrected frames were then summed for further analysis. Importantly, post-acquisition drift correction sometimes resulted in dark borders around the edges of the summed images (e.g., **Supplementary Figure 21**), as drift during data acquisition could cause portions of the initial FOV to move out of the imaged region.

Rate of CL detection

See **Supplementary Figure 22** for an overview of our method to calculate the rate of CL detection from LNPs. The method involved localizing a LNP in SE images and determining its emission characteristics at the corresponding location in the CL images as described below:

Localization of LNPs in SE images: The visibility of LNPs in the SE channel allowed us to precisely localize them. The position of a LNP in its SE image was determined by fitting a 2D Gaussian function to the image.

Number of photons: To determine the number of photons collected from the LNP, a 2D Gaussian function, $S(x, y)$, was fit to the summed CL image:

$$S(x,y) = b + a\exp\left[-\frac{(\mathrm{x}-\mathrm{x}_0)^2}{2\sigma_x^2} - \frac{(y-y_0)^2}{2\sigma_y^2}\right] = b + G(x,y) \quad 1$$

where (x_0, y_0), is the center position of the LNP, b is the background, a is amplitude, and σ_x and σ_y are the standard deviations of the 2D Gaussian function. $G(x, y)$ is the 2D Gaussian fit to the LNP without the background. Importantly, in this equation, $x0, y0$, σ_x and σ_y were constrained by the 2D Gaussian fit to the SE image.

The rate of CL detection (r), i.e., the number of photons collected from the LNP per second, was determined as

$$r = \frac{a}{\mathrm{d}t} \quad 2$$

where $\mathrm{d}t$ is the pixel dwell time. The amplitude of the 2D Gaussian function was used to determine the rate of CL detection, instead of the total number of photons in the CL image, because with our pixel size of 4–6 nm, a LNP was excited multiple times during image acquisition. The amplitude of the Gaussian corresponded to the most efficient excitation of the LNP (**Supplementary Figure 22**).

Signal-to-noise ratio

To determine the signal-to-noise ratio (SNR) of the CL image of a LNP, we used the following equation[1]:

$$\mathrm{SNR} = \frac{\mathrm{Signal}}{\mathrm{Noise}} = \frac{\sum G(x,y)}{\mathrm{Noise}} \quad 3$$

The Signal is the total number of photons collected from the LNP in a CL image. This number was obtained by summing the pixels of the fitted 2D Gaussian function. Only pixels within 2σ from the center (x_0, y_0) were included in the sum. Since the noise followed Poisson statistics (**Supplementary Figure 29**), for the i^{th} pixel it was:

$$\mathrm{Pixel\ noise} = N_i = \sqrt{I(x,y)} \quad 4$$

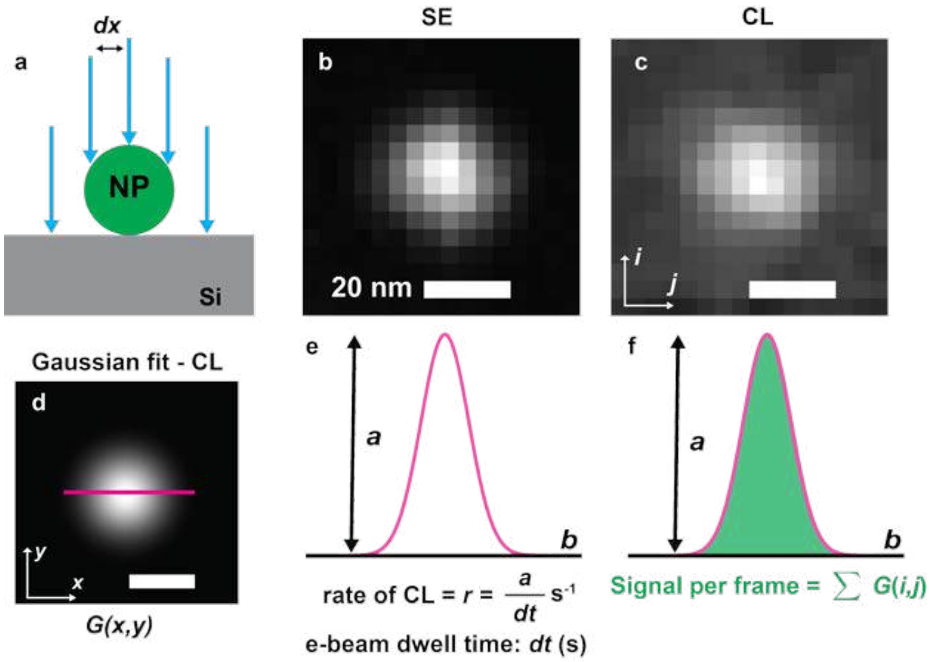

Supplementary Figure 22: CL data analysis. (a) An illustration showing that a LNP was excited multiple times during image acquisition. To achieve Nyquist sampling of the smallest LNPs, a pixel size (dx) of 4–6 nm was used in the experiments. **(b)** SE image of a LNP and **(c)** its corresponding CL image. **(d)** 2D Gaussian fit to the CL image from (c). **(e)** Cross-sectional profile of the 2D Gaussian fit taken along the red line shown in (d). The rate of CL was determined using the amplitude of the 2D Gaussian fit, which corresponded to the most efficient excitation of the LNP. **(f)** The number of photons collected from the LNP in a frame was determined by the area beneath the 2D Gaussian fit.

Here, $I(x,y)$ is the CL image intensity at pixel (x,y). To determine the total noise for the LNP, the noise was added in quadrature over the pixels within the 2σ radius of the LNP's center (x_0, y_0):

$$\text{Noise} = \sqrt{\sum N_i^2} = \sqrt{\sum I(x,y)} \qquad 5$$

Hence,

$$\text{SNR} = \frac{\sum G(x,y)}{\sqrt{\sum I(x,y)}} \qquad 6$$

Size of LNPs

The size of LNPs was determined from the oversampled SE images taken with the ZEISS Smart SEM software. These images had dimensions of 768 × 1024 pixels, with a pixel size of 0.2–0.3 nm. To determine the nanocrystal size, we fitted a 2D Gaussian function to the image of each LNP. Size was defined as the full width at half maximum (FWHM) of this fit. FWHM was calculated from the standard deviation of the Gaussian fit, as 2.355σ. Here σ is the average of the two standard deviations of the Gaussian fit.

It is worth noting that the oversampled images were acquired at fast scan speeds (1–3 µs pixel dwell time), three orders of magnitude faster than those used for CL imaging. Therefore, they did not suffer from the same charge buildup and subsequent drift, which would impact size determination. Additionally, more pixels per LNP improved Gaussian fitting.

Supplementary Note 16. Spectrum of holmium chloride

We prepared a sample of holmium chloride on a Si wafer and measured its spectrum using our spectrometer. Results are shown in **Supplementary Figure 23**. The spectrum of holmium chloride matched the spectrum of $NaHoF_4$ LNPs shown in **Supplementary Figure 34**. This result suggested that direct excitation of lanthanide ions, outside of the context of a nanocrystal, could produce CL.

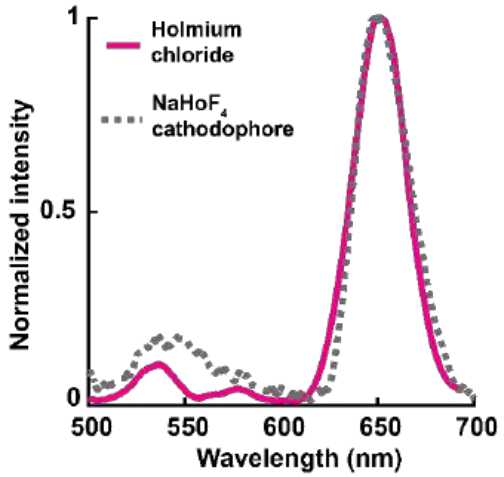

Supplementary Figure 23: CL from holmium chloride. CL spectum of holmium chloride matches the spectrum of $NaHoF_4$ LNPs. Source data are provided as a Source Data file.

Supplementary Note 17. Optimizing electron beam current for CL imaging

Rate of CL as a function of beam current: **Supplementary Figure 24a** shows the relationship between the CL detection rate from single LNPs and the electron beam current. The beam current was measured using a Faraday cup. The figure shows that there was no significant change in CL signal from LNPs for different beam current values. Different beam currents were obtained by changing the SEM aperture sizes, ranging from 20 μm to 120 μm, and by using “normal” and “high” current modes of the SEM.

However, with increased beam current, we also observed an increase in the apparent size of LNPs in SE images (**Supplementary Figure 24b**). This increase in size could be due to the deterioration of SEM resolution at higher beam currents (e.g., due to Coulombic effects), particularly when working with large apertures, at a long working distance, and imaging through the aperture of the parabolic mirror. **Supplementary Figure 24c** shows that the background CL increased for higher beam currents, indicating an increase in CL emission from Si as a function of beam current.

Electrobleaching and beam current: We also investigated the stability of $NaHoF_4$ LNPs for different values of beam current. Results are shown in **Supplementary Figure 25** for beam currents of 200 pA and 862 pA. The figure was generated by obtaining the average CL signal from LNPs of diameters between 17–30 nm (as measured from SE images) as a function of the cumulative pixel dwell time of the electron beam. It shows that the electrobleaching increased with an increase in beam current.

In summary, although a higher beam current provided more electrons to excite lanthanide ions in the LNPs, it also led to more electrobleaching of these ions. This effect resulted in a net decrease in the brightness of LNPs. Based on these results we used a beam current of 160–200 pA for our CL-SEM experiments.

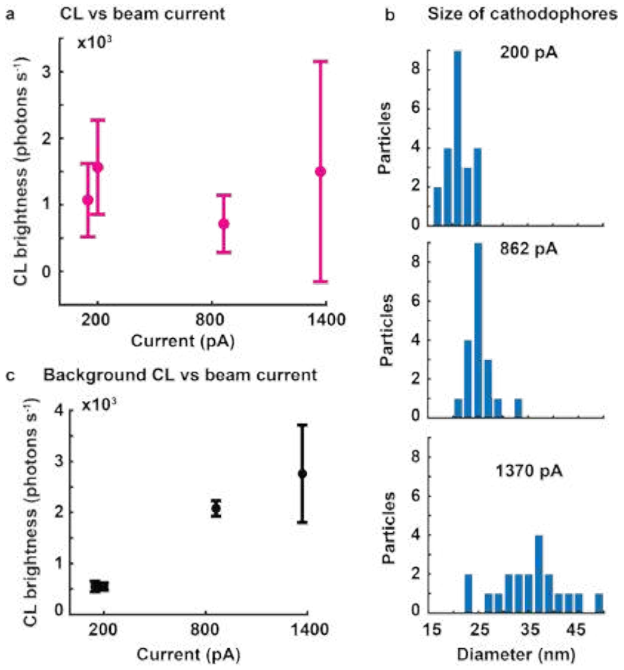

Supplementary Figure 24: CL brightness vs. beam current. (a) CL detection rate from $NaHoF_4$ LNPs as a function of electron beam current. CL was measured in the Ho^{3+} channel. At least 20 LNPs were imaged at each current. **(b)** Histograms of LNP sizes at different beam currents, as determined from SE images. An increase in size at higher beam currents could be due to deterioration in the resolution of the SEM at higher currents. This deterioration may be due to poor focusing of the electron beam when working with high currents (Coulombic effects), wide SEM apertures (required for high currents), long working distances, and a beam energy of only 3 keV. **(c)** Background CL from the Si substrate as a function of beam current, calculated from the 2D Gaussian fit of the LNP images analyzed in (a). Error bars in (a,c) show mean and standard deviation. Source data are provided as a Source Data file.

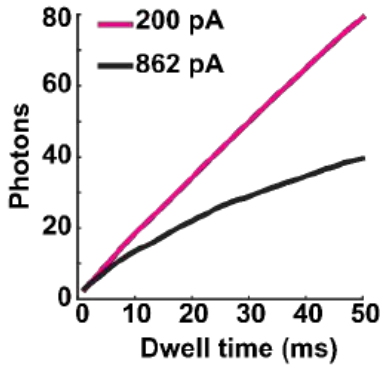

Supplementary Figure 25: CL vs. beam dwell time for different beam currents. Number of photons collected from $NaHoF_4$ LNPs as a function of total electron beam dwell time, for beam currents of 200 pA and 862 pA. 50 images were taken with a dwell time of 1 ms. Images with an effective dwell time of N ms were then generated by summing N consecutive frames. The number of photons collected from a LNP corresponded to the amplitude of its 2D Gaussian fit in a CL image. Higher nonlinearity for 862 pA indicates increased electrobleaching. CL was measured in the Ho^{3+} color channel. Source data are provided as a Source Data file.

Supplementary Note 18. Optimizing electron beam energy for CL imaging

Monte Carlo simulations: We performed Monte Carlo simulations in CASINO software[13] to determine the optimal electron beam energy to achieve efficient excitation of LNPs. A $NaHoF_4$ nanocrystal on a Si substrate was excited with different beam energies. 5,000 trajectories were simulated for each energy, and the energy deposited in the nanocrystal was calculated. Simulations were performed for two diameters of the nanocrystal: 20 nm and 30 nm.

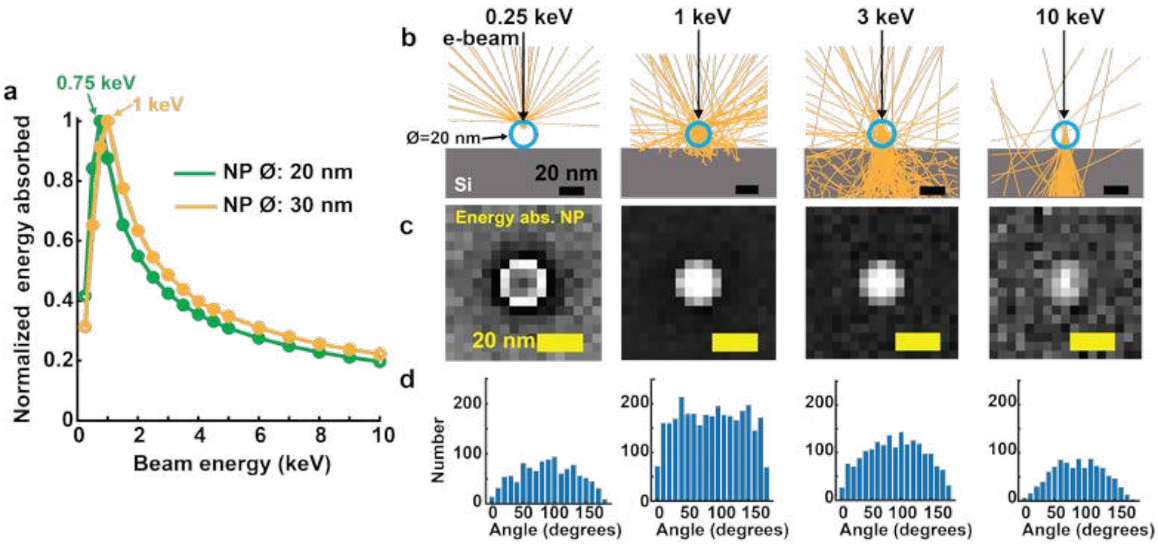

Supplementary Figure 26: CL vs. beam energy simulations. (a) Monte Carlo simulations to determine the energy absorbed by $NaHoF_4$ nanocrystals of two diameters, 20 nm and 30 nm, when excited by an electron beam of different energies. 5,000 trajectories were simulated for each energy. **(b)** Electron trajectories for the 20-nm $NaHoF_4$ nanocrystal (green circle) excited by the electron beam of different energies. The primary electron beam is shown as a black arrow. Stray electron trajectories are shown as orange lines. **(c)** Energy absorbed by the nanocrystal at each scanned position of the electron beam for the beam energies shown in (b). Each pixel of the image shows energy absorbed by the nanocrystal when the electron beam was focused at that position. **(d)** The angles at which electrons were emitted into vacuum after interaction with the sample. 90 degrees is antiparallel to the electron beam. Source data are provided as a Source Data file.

Results are shown in **Supplementary Figure 26a**. The optimal excitation energy was 0.75 keV for the 20 nm diameter nanocrystal, and 1 keV for the 30 nm diameter nanocrystal. At lower beam energies, the nanocrystal was not fully excited because the beam could not penetrate the nanocrystal. On the other hand, at higher beam energies, the beam went through the nanocrystal without exciting its entire volume (**Supplementary Figure 26b**).

Supplementary Figure 26d shows angles at which electrons traveled in vacuum when the 20-nm nanocrystal was excited by the electron beam. At 1 keV, the electrons emerged nearly uniformly at all angles (90 degrees is antiparallel to the electron beam). In contrast, at both lower beam energies (0.25 keV in the figure) and higher beam energies (10 keV in the figure), the angles were arranged in a cosine-like distribution. This was because the high-energy beam penetrated the substrate, and the electrons scattered in directions away from the beam remained trapped within the substrate. Similarly, for lower beam energies, such electrons were trapped within the nanocrystal.

Experiments to determine the optimal beam energy: **Supplementary Figure 27a** shows CL from $NaHoF_4$ LNPs of 20–25 nm diameter at different beam energies. For energies ≥3 keV, the CL signal did not change significantly. However, we observed a reduction in the CL signal for beam energies below 3 keV. This result was different from Monte Carlo simulations. The contradiction was due to the sub-optimal performance of our SEM when low beam energies were used to image at long working distances through the 500-µm-diameter aperture of the parabolic mirror. A long working distance (≈6.5 mm) was needed for CL imaging because the parabolic mirror was installed between the electron gun and the sample. This suboptimal performance was also seen when we plotted the rate of CL detection from LNPs as a function of their size (**Supplementary Figure 27b**). We obtained a similar CL signal for the beam energies of 3 keV and 6 keV. However, at 2.5 keV the CL signal reduced for a given LNP size. We attributed this reduction to the suboptimal focusing of the electron beam, which is consistent with the increase in LNP size shown in **Supplementary Figure 27b**.

Although the CL signal did not change significantly for the beam energies of 3–8 keV, the background CL from the Si substrate increased (**Supplementary Figure 27c**). This was because more electrons penetrated the substrate at higher beam energies. Moreover, the contrast generated by the nanocrystals decreased at high beam energies as shown in **Supplementary Figure 27d.** This decrease in contrast is explained by Monte Carlo simulations, which showed that, at high beam energies, many electrons passed through the LNPs ballistically, without scattering. Based on these results, we chose 3–4 keV as the optimal beam energy for our CL-SEM experiments.

Energy absorbed by LNPs of different sizes: We performed Monte Carlo simulations to determine the energy absorbed by LNPs as a function of their size under different beam energies. $NaHoF_4$ nanocrystals with diameters of 5–100 nm were simulated. The electron beam energy was varied from 0.5–10 keV. The beam diameter was set to 4 nm. 5,000 trajectories were simulated for each condition. Results are shown in **Supplementary Figure 28a**. The energy absorbed by the nanocrystal increased as a function of its size, up to the point where the beam interaction volume matched the size of the nanocrystal. Beyond this point, an increase in the nanocrystal diameter did not change the interaction volume inside the nanocrystal, and therefore the energy absorbed by the nanocrystal did not change (**Supplementary Figure 28b**, top row). For example, for 0.5 keV and 1 keV, the energy absorbed by the nanocrystal plateaued beyond diameters of 15 nm and 40 nm respectively. However, for energies >1 keV,

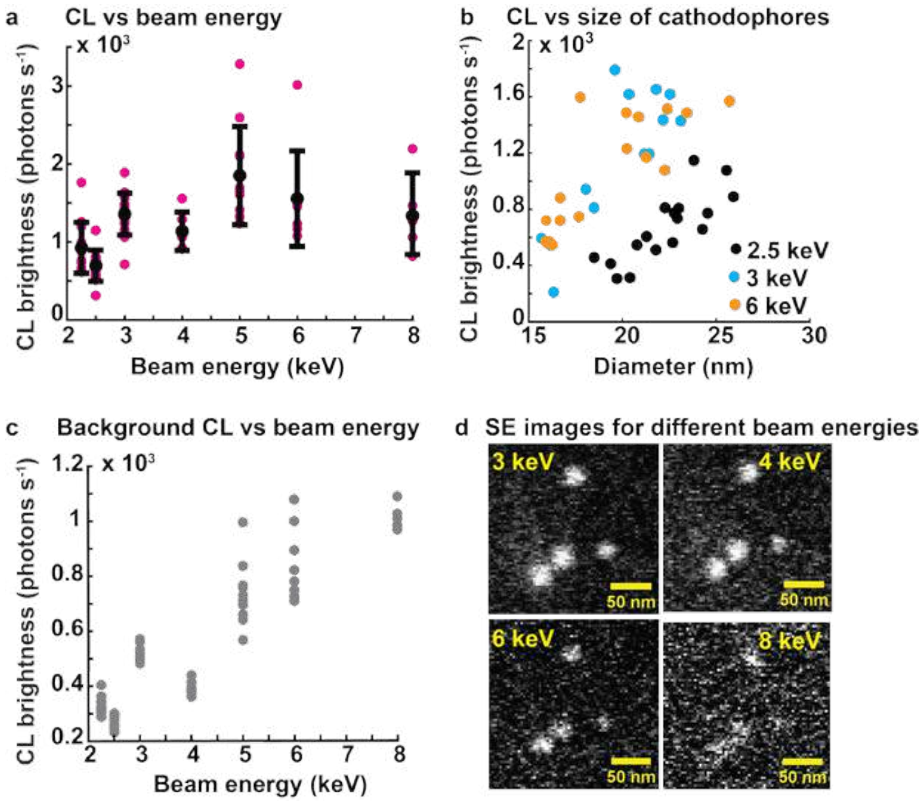

Supplementary Figure 27: CL from LNPs and Si as a function of beam energy. (a) CL brightness of $NaHoF_4$ LNPs as a function of electron beam energy. The diameter of LNPs was 20–25 nm. No significant change in the rate was observed for beam energies ≥3 keV. CL was measured in the Ho^{3+} channel. At least 14 LNPs were imaged at each beam energy. **(b)** CL brightness as a function of LNP size for three beam energies: 2.5 keV, 3 keV, and 6 keV. The lower CL detection rate at 2.5 keV was likely due to the loss of SEM resolution when imaging at long working distances (>6 mm) using low beam energies. **(c)** Background CL from Si substrate as a function of beam energy, calculated from the 2D Gaussian fit of the LNP images analyzed in (a). **(d)** SE images of the same LNPs for different beam energies. At higher energies, the contrast was reduced because many electrons passed through the LNPs ballistically without scattering. Error bars in (a,c) show mean and standard deviation. Source data are provided as a Source Data file.

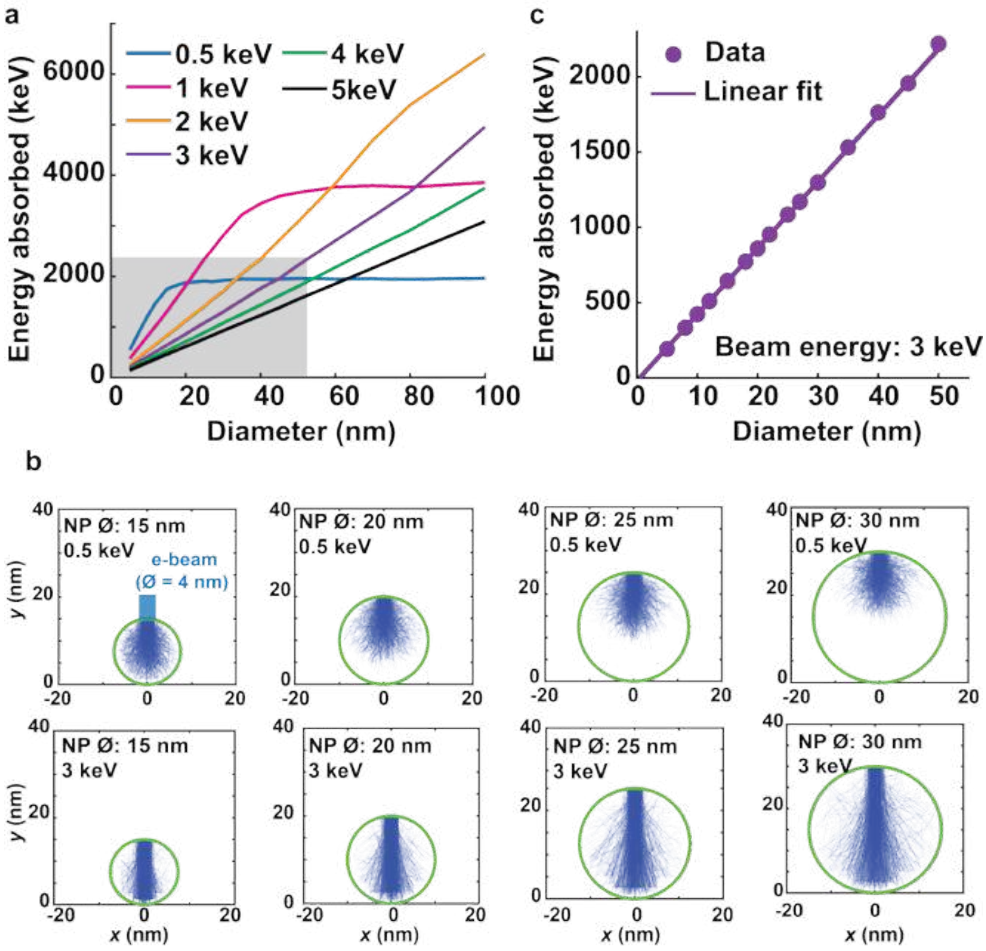

Supplementary Figure 28: CL vs. LNP diameter for different beam energies. (a) Monte Carlo simulations to determine the energy absorbed by $NaHoF_4$ nanocrystals of different sizes when excited by different electron beam energies. Energy absorbed by the nanocrystal increased monotonically as a function of its size until the beam interaction volume matched the size of the nanocrystal. Beyond this size, the energy absorbed by the nanocrystal did not change with an increase in the nanocrystal diameter because the interaction volume inside the nanocrystal did not change. 5,000 trajectories were simulated for each condition. **(b)** Electron trajectories within the nanocrystal for four different sizes (15 nm, 20 nm, 25 nm, and 30 nm), for beam energies of 0.5 keV (top row) and 3 keV (bottom row). **(c)** Focusing on the shaded region in (a) for 3 keV: energy absorbed by nanocrystals of different sizes when excited by a 3 keV electron beam. The data (circles) fit well with a straight line, indicating a linear relationship between the energy absorbed by nanocrystals as a function of size at 3 keV excitation beam energy. Source data are provided as a Source Data file.

which optimally excited nanocrystals with diameters >100 nm, a monotonic increase in the energy absorbed by the nanocrystal was observed for all the simulated sizes.

When the beam energy was significantly higher than the optimal energy, we observed a linear relationship between the energy absorbed by the nanocrystal and its size. This linear trend was observed because at such energies, the entire volume of the nanocrystal was not excited. Instead, the overlap between the electron interaction volume and the volume of the nanocrystal could be approximated by a vertical cylinder with a diameter corresponding to the size of the primary electron beam and the length given by the z-dimension (height) of the nanocrystal. So, the height of the nanocrystal primarily determined the energy absorbed by the nanocrystal (**Supplementary Figure 28b**, bottom row).

Supplementary Figure 28c shows results of exciting nanocrystals with diameters ranging from 5–50 nm, with a 3 keV beam. We observed a linear increase in the energy absorbed by the nanocrystal as a function of its size. Note that we used a beam energy of 3 keV

in our CL experiments. Assuming that CL emission is proportional to the energy absorbed by the nanocrystal (true for fluorescence in the linear regime within a factor given by the quantum yield), we expected a linear increase in the CL from LNPs as a function of their size. **Fig. 4a** experimentally confirmed that the CL increased linearly as a function of LNP size.

Supplementary Note 19. Background from Si substrate

CL signal from Si substrate: We used Si wafers as a substrate for CL imaging due to its flatness, conductivity, and low CL. The Si substrate had a wide CL emission spectrum and led to ≈350 detected photons s^{-1} on average in Ho^{3+} and Tb^{3+} color channels and ≈400 detected photons s^{-1} in the Dy^{3+} color channel as shown in **Supplementary Figure 29a**. This CL from Si appeared as background when LNPs were imaged.

CL from Si increased linearly as a function of electron beam dwell time. Additionally, the mean of the CL signal matched its variance for all dwell times, which was consistent with Poisson statistics of the noise (**Supplementary Figure 29b–d**). For each dwell time, mean and variance were calculated from multiple pixels in the CL image of the Si substrate.

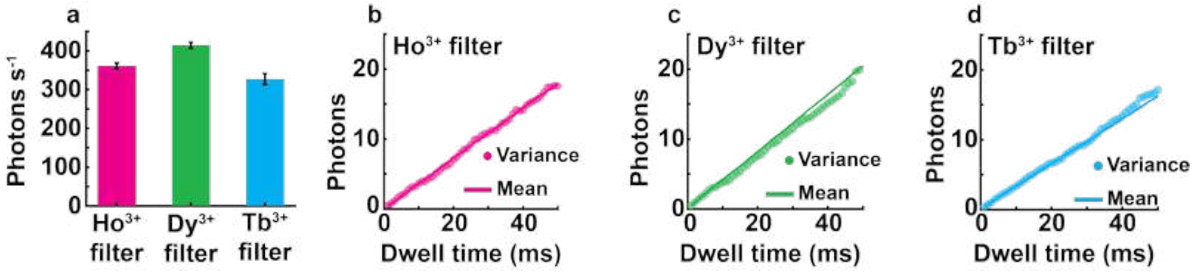

Supplementary Figure 29: CL from Si. (a) CL from Si across different spectral filters. Error bars show the standard deviation in the average CL signal collected from four different regions of the Si wafer. CL was collected with an effective beam dwell time of 50 ms (50 frames with 1 ms dwell time each). **(b–d)** Mean and variance of CL signal from Si substrate as a function of the effective beam dwell time across Ho^{3+}, Dy^{3+}, and Tb^{3+} channels. Similar mean and variance suggested that the signal followed Poisson distribution. Source data are provided as a Source Data file.

Simulations to analyze the detection limit: We conducted simulations to determine the minimum CL emission rate required for the detection of CL from LNPs. CL images were simulated for the typical electron beam dwell time of 50 ms. The background was set to 25 counts per pixel (500 photon s^{-1} $pixel^{-1}$) with a Poisson distribution to match the CL from Si across our band-pass filters, as discussed above. CL signal from LNPs was modeled as a 2D Gaussian function. LNPs with varying levels of CL signal were simulated by changing the amplitude of the simulated 2D Gaussian function. Simulated images were analyzed using the image processing protocol discussed in **Supplementary Figure 22**. As expected, the SNR of CL images increased with an increase in the number of photons collected from LNPs as shown in **Supplementary Figure 30a,b**. **Supplementary Figure 30e** shows representative simulated images with different SNRs.

To determine the detection limit, we analyzed images without LNPs. In this case, the simulated images contained only the background from the Si substrate. Analysis of these images corresponded to fitting a 2D Gaussian to the background, where the amplitude of the fitted Gaussian was determined by the background noise (i.e., Poisson noise from Si substrate). The histogram in **Supplementary Figure 30c** shows the distribution of SNRs for images without the LNPs. The distribution had a $mean + 2\sigma$ value of 2.2, which we used as the lower limit for the detection of LNPs. Based on this criterion, we needed at least 8 photons (160 photons s^{-1}) from a LNP to detect it with 95% confidence (**Supplementary Figure 30d**). For CL detection rates exceeding 160 photons s^{-1}, we could detect the LNP in at least 95 out of 100 iterations.

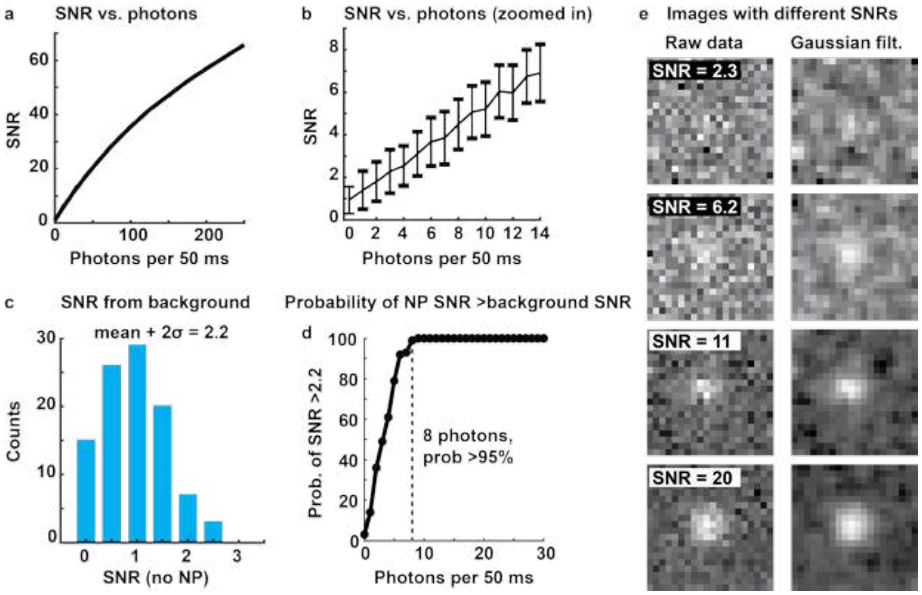

Supplementary Figure 30: Simulations to determine the detection limit of LNPs on Si substrate. (a) SNR of simulated CL images as a function of the number of photons collected from nanocrystals, given a beam dwell time of 50 ms. **(b)** A magnified region of the plot in (a). Error bars show the mean and standard deviation for SNR across 100 frames. Images were generated with a Poisson background with an average of 25 photons to match the CL from Si at our typical beam dwell time of 50 ms. Nanocrystals were simulated as a 2D Gaussian function above the background. Nanocrystals with different numbers of photons were generated by changing the amplitude of the 2D Gaussian. 100 images were simulated for each photon count. **(c)** Histogram of SNRs obtained by fitting a 2D Gaussian function to the background across 100 simulated images. **(d)** Probability of obtaining an SNR >2.2 for different numbers of photons collected from nanocrystals. The number 2.2 corresponds to the $(mean + 2\sigma)$ of the SNR distribution in (c). **(e)** Simulated images of nanocrystals at different SNRs and their respective Gaussian filtered images ($\sigma = 0.7\ pixels$). Source data are provided as a Source Data file.

Fig. 4a shows that the detection rate of 160 photons s^{-1} corresponds to a diameter of ≈15 nm for Ho^{3+}, Dy^{3+} and Tb^{3+} LNPs, which was also the x-intercept of the linear fits shown in the figure. These results confirmed that the background from the Si substrate dictated the minimal photon count necessary for the statistically significant detection of CL from LNPs.

Supplementary Note 20. $NaGdF_4$ nanocrystals as a control sample

Significance of using $NaGdF_4$ nanocrystals as a control: Background CL from Si substrate determined the minimum brightness of LNPs required for their detection. However, detection of a LNP in a specific spectral channel could also be due to nonlocal excitations. We took steps to mitigate these excitations, which included optimizing the sample preparation protocol and optically isolating the emission path inside the SEM with a lens tube.

Nevertheless, some nonlocal CL remained, especially for larger LNPs, and it was important to ensure that it did not impact our analysis for the classification of LNPs across all sizes. One potential cause of this nonlocal signal could be the enhanced CL from the Si substrate: excitation of LNPs led to a higher number of stray electrons, which could interact with the substrate. And the Si substrate, as we learned from **Supplementary Figure 24c**, showed brighter luminescence at larger beam currents. Additionally, even with the lens tube optically isolating the emission path inside the SEM, some nonlocal CL could potentially reach the PMTs.

As discussed earlier, LNPs were composed of high-Z elements and produced more stray electrons than the Si substrate. Therefore, it was important for the control to match the characteristics (shape, size, and atomic number (Z)) of the LNPs, while being non-cathodoluminescent to ensure that it only appeared luminescent due to nonlocal excitation. $NaGdF_4$ particles met these criteria, so we used them as a control instead of Si.

SNR of $NaGdF_4$ nanocrystals: $NaGdF_4$ nanocrystals were imaged across different color filters. The SNR was calculated for these images and results are shown in **Supplementary Figure 31a,e,i**. The figure shows that the SNR from $NaGdF_4$ nanocrystals increased with an increase in their size, which could be a result of increased nonlocal excitation due to a higher number of stray electrons emitted from larger nanocrystals. For bona fide LNPs (e.g., $NaHoF_4$) to be detected in their respective channels, they had to be brighter than the $NaGdF_4$ nanocrystals.

Smallest LNPs classified in our CL-SEM experiments: Next, we determined the minimum size of LNPs that could be classified in our CL-SEM experiments. To this end, we compared the SNR from CL images of $NaHoF_4$, $NaDyF_4$, and $NaTbF_4$ LNPs of different sizes to the SNR from $NaGdF_4$ particles of the same size. Results are shown in **Supplementary Figure 31b,f,j**. LNPs were classified as containing a specific dopant if the SNR of their CL images was higher than $mean + 2\sigma$ of the SNR obtained from $NaGdF_4$ nanocrystals of the same size. This

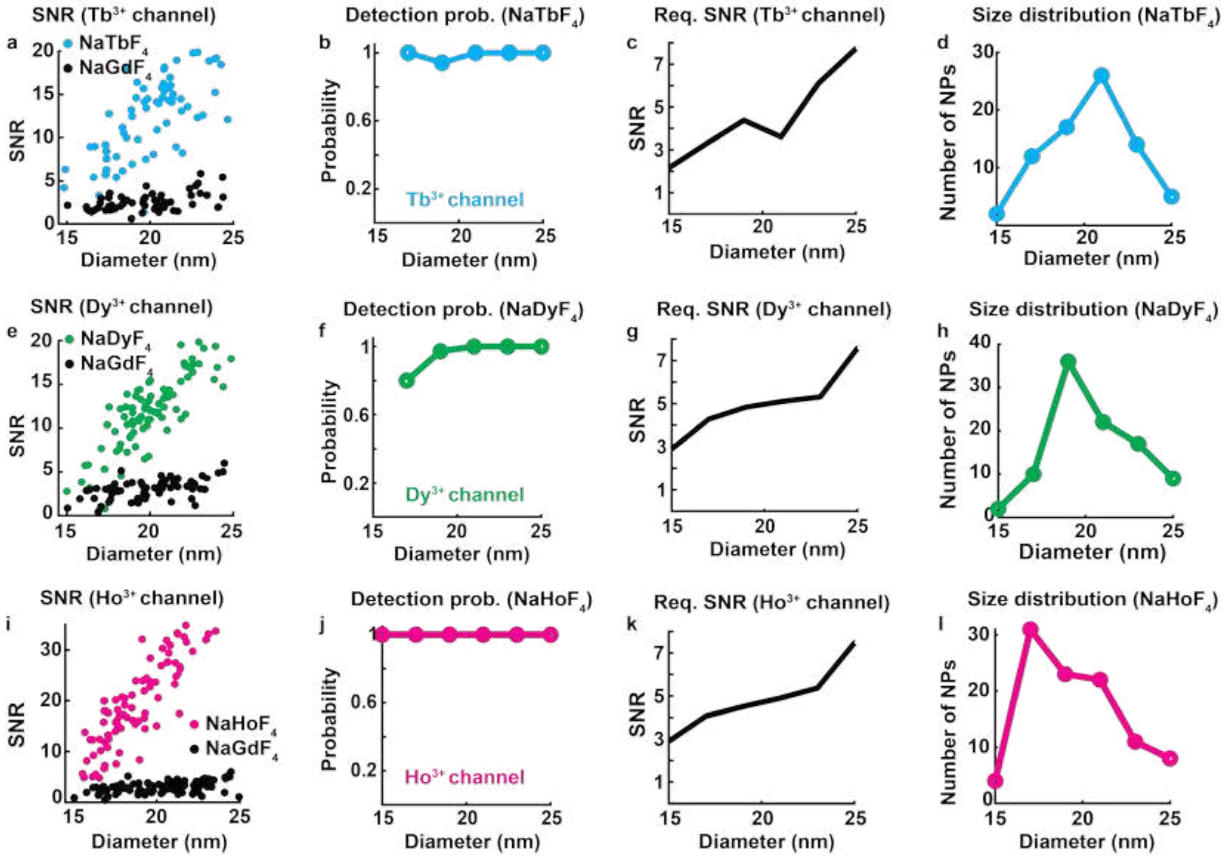

Supplementary Figure 31: SNR and detection probability for LNPs. (a) SNR from $NaTbF_4$ and $NaGdF_4$ nanocrystals in the Tb^{3+} color channel as a function of their size. **(b)** Probability of detecting $NaTbF_4$ LNPs in the Tb^{3+} color channel as a function of their size. **(c)** Minimum SNR required to detect a particle in the Tb^{3+} channel, determined as $(mean + 2\sigma)$ of the SNR distribution from $NaGdF_4$ nanocrystals in the Tb^{3+} color channel. **(d)** Size distribution of $NaTbF_4$ LNPs used in the analysis in (a) and (b). **(e)** SNR from $NaDyF_4$ and $NaGdF_4$ nanocrystals in the Dy^{3+} color channel as a function of size. **(f)** Probability of detecting $NaDyF_4$ LNPs in the Dy^{3+} color channel as a function of their size. **(g)** Minimum SNR required to detect a particle in the Dy^{3+} channel, determined as $(mean + 2\sigma)$ of the SNR distribution from $NaGdF_4$ nanocrystals in the Dy^{3+} color channel. **(h)** Size distribution of $NaDyF_4$ LNPs used in the analysis in (e) and (f). **(i)** SNR from $NaHoF_4$ and $NaGdF_4$ nanocrystals in the Ho^{3+} color channel as a function of their size. **(j)** Probability of detecting $NaHoF_4$ LNPs in the Ho^{3+} color channel as a function of their size. **(k)** Minimum SNR required to detect a particle in the Ho^{3+} channel, determined as $(mean + 2\sigma)$ of the SNR distribution from $NaGdF_4$ nanocrystals in the Ho^{3+} color channel. **(l)** Size distribution of $NaHoF_4$ LNPs used in the analysis in (i) and (j). (b,f,j) The probability of detecting LNPs was calculated from the fraction of LNPs with an SNR higher than the $(mean + 2\sigma)$ of the SNR distribution from $NaGdF_4$ nanocrystals of the same size and in the corresponding color channel, which are shown in (c,g,k). In all plots, diameter was measured as the FWHM of a LNP in its SE image. Source data are provided as a Source Data file.

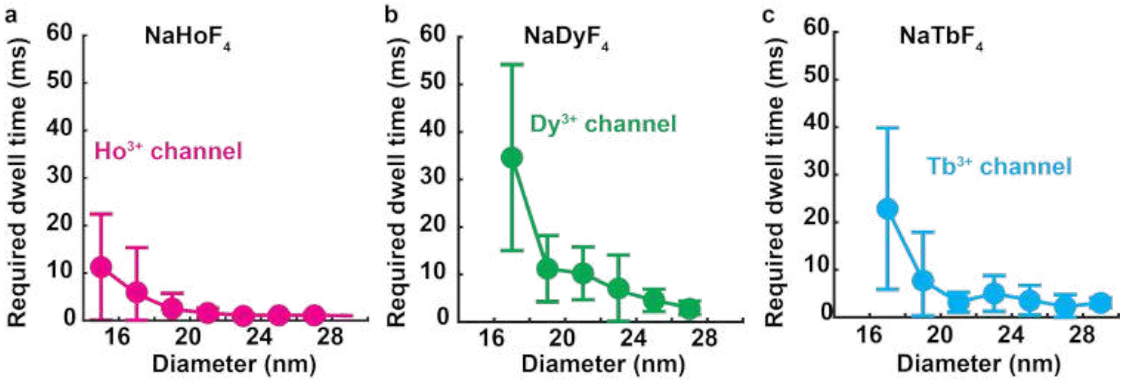

Supplementary Figure 32: Required beam dwell time for LNP detection. (a) Effective beam dwell time required to detect $NaHoF_4$ LNPs in the Ho^{3+} color channel. **(b)** Effective beam dwell time required to detect $NaDyF_4$ LNPs in the Dy^{3+} color channel. **(c)** Effective beam dwell time required to detect $NaTbF_4$ LNPs in the Tb^{3+} color channel. (a–c) 50 frames were acquired with a beam dwell time of 1 ms. Images with an effective dwell time of N ms were generated by summing N consecutive frames. LNPs were detected if their SNR was higher than $(mean + 2\sigma)$ of the SNR distribution from same-sized $NaGdF_4$ nanocrystals, acquired using the same dwell time and in the corresponding color channels. Error bars show mean and standard deviation of the data. Number of imaged LNPs are shown in Supplementary Figure 31 (d,h,l). Source data are provided as a Source Data file.

limit is shown in **Supplementary Figure 31c,g,k**. Each dopant was analyzed in the CL channel matched to its emission peak.

We found that we could classify $NaHoF_4$, $NaDyF_4$, and $NaTbF_4$ down to 15 nm diameter. $NaHoF_4$ could be detected with 100% probability across all sizes. For $NaDyF_4$, a 100% detection probability was achieved for LNPs exceeding 16 nm. **Supplementary Figure 31d,h,l** show the size distributions of LNPs used in the analysis. It is important to note that ≈15 nm was the smallest diameter of nanocrystals visible in our SE images. This could be because at 3 keV beam energy, LNPs smaller than 15 nm did not produce enough electron signal to be detected.

Frames required for detection: We also determined the number of frames (1 ms pixel dwell time per frame) required for the classification of LNPs, i.e., the number of frames required to achieve the SNR essential for classification. Results are shown in **Supplementary Figure 32.** The figure shows that the effective dwell time of 50 ms, as used in our experiments, was sufficient to detect LNPs of all sizes.

Supplementary Note 21. Relationship between CL signal and LNP size

Fig. 4a demonstrated a monotonic increase in the brightness of single LNPs as a function of their diameter in the absence of nonlocal excitation. In the figure, we showed a linear fit to the data, in agreement with the Monte Carlo simulations in **Fig. 1c** and **Supplementary Figure 28**. In this note, we examine whether a nonlinear relationship might better describe the observed trend.

In **Supplementary Figure 33** we show linear, quadratic, and cubic fits for $NaHoF_4$ LNPs in the Ho^{3+} color channel. We assessed the quality of each fit using the root mean square error (RMSE), calculated as:

$$\mathrm{RMSE} = \sqrt{\frac{\sum(f_i - y_i)^2}{N}} \qquad 7$$

Here, f_i and y_i are the i^{th} fitted and raw data values respectively, and N is the total number of observations.

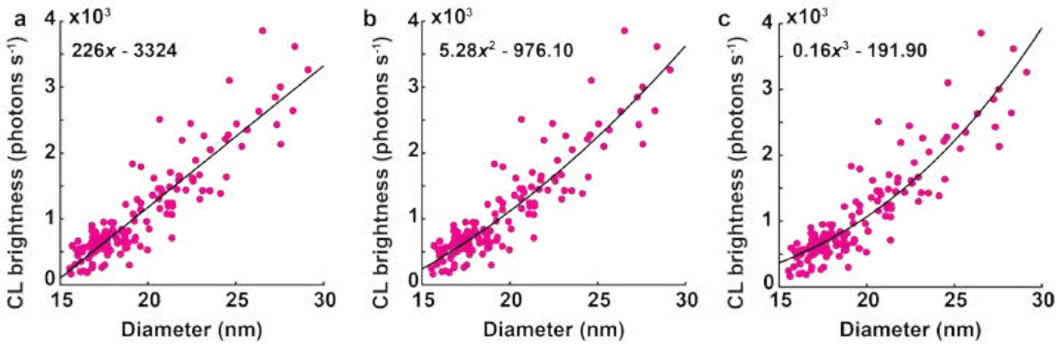

Supplementary Figure 33: Comparison of linear and nonlinear fits to CL vs. LNP size data. (a) Linear ($r = mx + b$), **(b)** quadratic ($r = mx^2 + b$), and **(c)** cubic ($r = mx^3 + b$) fits to the CL brightness vs. LNP diameter for $NaHoF_4$ LNPs in the Ho^{3+} channel. r is CL brightness in photons s^{-1}, x is the diameter of LNPs in nm, b is the *y*-intercept in photons s^{-1}, m is the co-efficient of x in (a) photons s^{-1} nm^{-1}, (b) photons s^{-1} nm^{-2}, and (c) photons s^{-1} nm^{-3}. Note that the factor 10^3 in the *y*-axis was included in all fits.

The RMSE values were similar for the three fits. For the linear fit, the RMSE was 394.2 photons s^{-1}. For the quadratic and cubic fits, the RMSEs were 389.6 photons s^{-1} and 395.4 photons s^{-1} respectively.

Since we did not observe any significant improvement in the fit quality when using nonlinear models, for simplicity, and in agreement with the predictions from Monte Carlo simulations, we used a linear fit to describe the data. However, it is important to note that we cannot entirely dismiss the possibility of a nonlinear dependence. Such a relationship might suggest that absorbed energy, which was used as a proxy for CL signal in the simulations, does not fully account for CL brightness. Additional factors could include efficient excitation of CL by low-energy secondary electrons or contributions from the electric field of high-energy electrons—effects not captured by the Monte Carlo simulations.

The difference between the linear fit values in this note and in **Fig. 4a** (Ho^{3+} channel) was due to the difference in the fitting approach. In **Fig. 4a**, we used the *robustfit()* function in MATLAB, which minimizes the impact of outliers during linear regression. In contrast, the analysis here employed the *fit()* function, without the robust option, to ensure a fair comparison between different models. Moreover, this analysis only included LNPs with diameters >15 nm, whereas the fit presented in the main text used the entire dataset.

Supplementary Note 22. Single-particle CL spectra

To obtain single-LNP spectra, we prepared a sparse sample of LNPs containing a specific dopant. CL from the LNP was collected by repeatedly scanning the electron beam over it. The CL emitted by the LNP was collected by the parabolic mirror and projected onto the spectrometer: the light was focused onto the camera through the diffraction grating (see **Supplementary Figure 6**). Spectra were extracted from images taken with the sCMOS camera. The spectral information resided in the first diffraction order of the grating. Spectra were obtained by plotting the intensity of pixels in the first diffraction order as a function of distance from the center of the zeroth order. This distance was then converted to wavelength using a calibration sample with a known spectrum. A moving average filter was applied to the distance to remove high-frequency noise from the spectra.

Fig. 4f shows representative spectra of single LNPs. In **Supplementary Figure 34** more examples of single-particle spectra are provided for $NaHoF_4$, $NaDyF_4$, $NaTbF_4$, and $NaSmF_4$ LNPs. The figure shows that the spectra of single LNPs matched their ensemble spectra, confirming the spectral stability of LNPs at the single-particle level. This spectral stability allowed us to specifically select filters matched to the primary emission peaks of the LNPs.

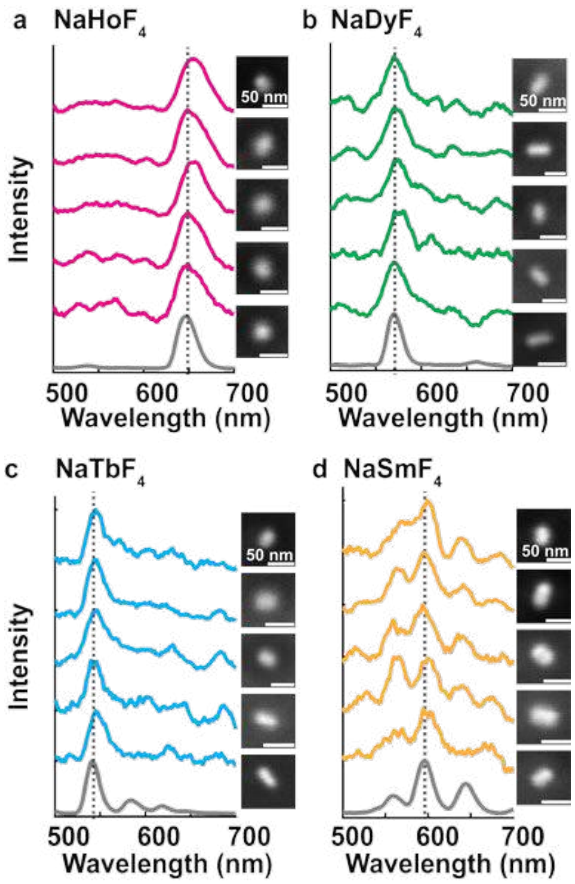

Supplementary Figure 34: Single-particle spectra. (a–d) Single-particle spectra of $NaHoF_4$, $NaDyF_4$, $NaTbF_4$, and $NaSmF_4$ LNPs respectively. Spectra were acquired using our custom spectrometer (**Supplementary Figure 6**) by continously scanning a 100 nm × 100 nm^2 region around the LNPs. Ensemble spectra of the LNPs are also shown (gray lines). Single-particle spectra of LNPs matched their ensemble spectra. Dotted lines indicate the positions of the primary emission peaks of LNPs. Source data are provided as a Source Data file.

Supplementary Note 23. Electrobleaching

Supplementary Figure 35 shows CL collected from $NaHoF_4$ LNPs in a CL image. CL from three different size ranges is shown. The electron beam dwell time was 5 ms. The CL signal in subpanels a–c corresponds to the total CL signal collected from LNPs within a frame. It was determined by calculating the area under the 2D Gaussian fit to the CL image of the LNP in the Ho^{3+} color channel. The figure shows that the detected CL from LNPs decreased over time, which was indicative of electrobleaching. For each size range, CL from $NaGdF_4$ nanocrystals of the same size is also shown. Despite the electrobleaching, CL from $NaHoF_4$ LNPs was higher than that of $NaGdF_4$ for all sizes and dwell times.

Supplementary Figure 36 shows CL collected from $NaDyF_4$ LNPs of three different sizes. Unlike $NaHoF_4$, $NaDyF_4$ displayed minimal electrobleaching, even for smaller, sub-20-nm LNPs. Since $NaDyF_4$ LNPs emitted fewer photons than $NaHoF_4$, their CL signal in some frames was comparable to the CL from the control, $NaGdF_4$. However, CL from $NaDyF_4$ for a dwell time of 50 ms (**Supplementary Figure 36d–f**) was higher than $NaGdF_4$, enabling their classification down to ≈16 nm. These results show the effect of the dopant type on electrobleaching. However, the microscopic mechanism behind this difference remains to be understood.

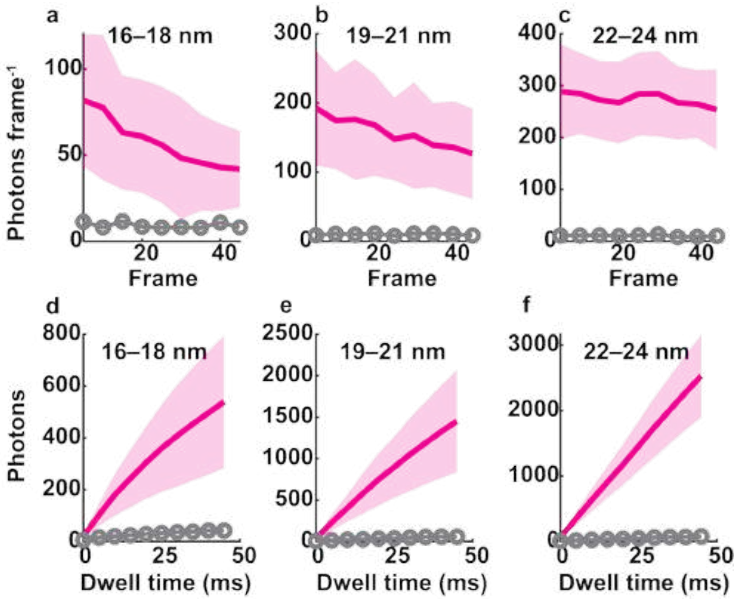

Supplementary Figure 35: Electrobleaching of $NaHoF_4$ LNPs. (a–c) Photons frame^{-1} collected from $NaHoF_4$ for three different LNP diameters. Photons frame^{-1} obtained from $NaGdF_4$ are also shown for a comparison (gray). Images had an effective beam dwell time of 5 ms. **(d–f)** Cumulative photons collected from $NaHoF_4$ LNPs in a CL image for different beam dwell times. Images were obtained by summing photons frame^{-1} shown in (a–c). In (a–f), photons frame^{-1} correspond to the integrated area under the 2D Gaussian fit to the CL image of LNPs. CL was measured in the Ho^{3+} color channel. In (a–f), solid lines and shaded regions correspond to the mean and standard deviation of the data. Source data are provided as a Source Data file.

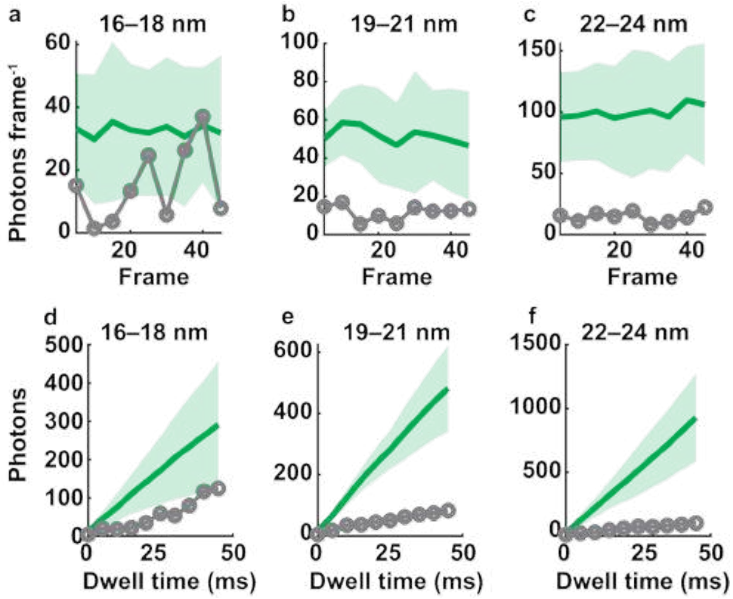

Supplementary Figure 36: Electrobleaching of $NaDyF_4$ LNPs. (a–c) Photons frame^{-1} collected from $NaDyF_4$ for three different LNP diameters. Photons frame^{-1} obtained from $NaGdF_4$ are also shown for a comparison (gray). Images had an effective beam dwell time of 5 ms. **(d–f)** Cumulative photons collected from $NaDyF_4$ LNPs in a CL image for different beam dwell times. Images were obtained by summing photons frame^{-1} shown in (a–c). In (a–f), photons frame^{-1} correspond to the integrated area under the 2D Gaussian fit to the CL image of LNPs. CL was measured in the Dy^{3+} color channel. In (a–f), solid lines and shaded regions correspond to the mean and standard deviation of the data. Source data are provided as a Source Data file.

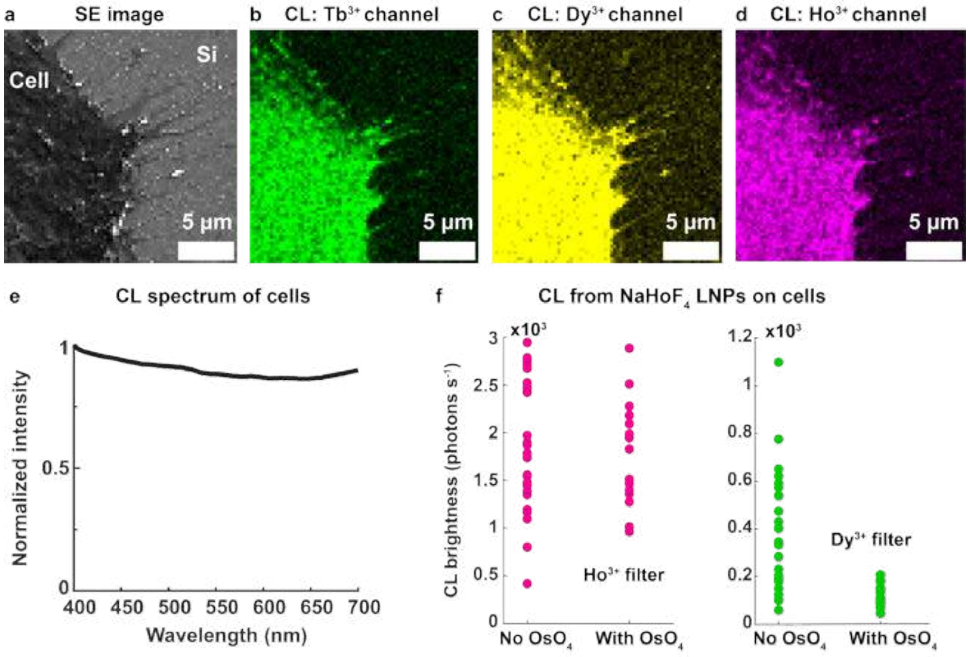

Supplementary Figure 37: Auto-CL from cells. (a) SE image of a HEK293T cell on a Si wafer. **(b,c,d)** Auto-CL from the cell in (a) in the Tb^{3+}, Dy^{3+}, and Ho^{3+} color channels respectively. **(e)** Quantum-efficiency-corrected CL spectrum of the auto-CL of HEK293T cells. (f) CL from $NaHoF_4$ LNPs on cells in the Ho^{3+} and Dy^{3+} color channels, with and without OsO_4 treatment. Source data are provided as a Source Data file.

Supplementary Note 24. Imaging single LNPs in a biological sample

Sample preparation for mammalian cells: Cultured cells were prepared for CL imaging via osmium tetroxide (OsO_4) treatment and hexamethyldisilazane (HMDS) drying based on previously reported protocols[14,15]. HEK293T cells were cultured in 50/50 DMEM/F-12 media with 10% fetal bovine serum and 1% penicillin/streptomycin. Cells were dissociated using 0.25% trypsin in PBS, then seeded on plasma-cleaned Si wafers. After adhering to the Si wafers overnight, cells were washed twice with PBS and fixed with 4% formaldehyde, 0.2% glutaraldehyde in PBS, pH 7.4 for 15 min with gentle agitation. Cells were washed three times with PBS and incubated in 1% OsO_4 in PBS for 10 min with gentle agitation. Then, cells were washed with MilliQ water for 2 hours with gentle agitation, replacing water every 15 min. Cells were gradually transitioned into ethanol by increasing from 10% ethanol to 100% ethanol using steps of 10%, with 5 min of gentle agitation between each step. Upon reaching 100% ethanol, cells were gently agitated twice for 20 min with fresh ethanol each time. Next, cells were gradually transitioned into HMDS by increasing from 25% HMDS in ethanol to 100% HMDS using steps of 25%, with 5 min of gentle agitation between each step. When 100% HMDS was reached, cells were gently agitated twice for 20 min with fresh HMDS each time. Finally, the majority of HMDS volume was removed from the cells to leave a thin layer of HMDS, and cells were air dried. If appropriate, 5 µL of washed, n-hexane-suspended single LNPs was drop-cast onto the cells. Finally, cells were sputter coated with a 2.5-nm-thick layer of 80:20 Pt:Pd to prevent charging during CL-SEM imaging.

Auto-CL from cells and its impact on single-particle imaging: Auto-CL from cells had a broadband spectrum (**Supplementary Figure 37**). This auto-CL not only increased background signal but also led to nonlocal excitation of cells via stray electrons from LNPs, as discussed in Fig. 2 of the main text. This led to erroneous signal from LNPs. The effect is illustrated in **Supplementary Figure 37f**, where $NaHoF_4$ LNPs were imaged on cells. In the absence of OsO_4 treatment, $NaHoF_4$ LNPs also appeared to emit in the Dy^{3+} channel due to

nonlocal excitation of cells. This effect was less apparent in the Ho^{3+} channel due to a distribution of CL signal from the emitting LNPs (Fig. 4 of the main text). This erroneous signal disappeared following OsO_4 treatment.

Size of LNPs after sputter coating: Sputter coating was required to image cells in our CL-SEM to minimize charge buildup. The cells were coated with a 2.5-nm-thick layer of 80:20 Pt:Pd. LNPs were added to cells prior to sputter coating.

Although the resolution of our CL-SEM imaging was still defined by the size of the focused electron beam, the sputter coating increased the apparent size of the LNPs. **Supplementary Figure 38** compares the sizes of the LNPs on a Si substrate without coating, on a coated Si substrate, and on coated mammalian cells.

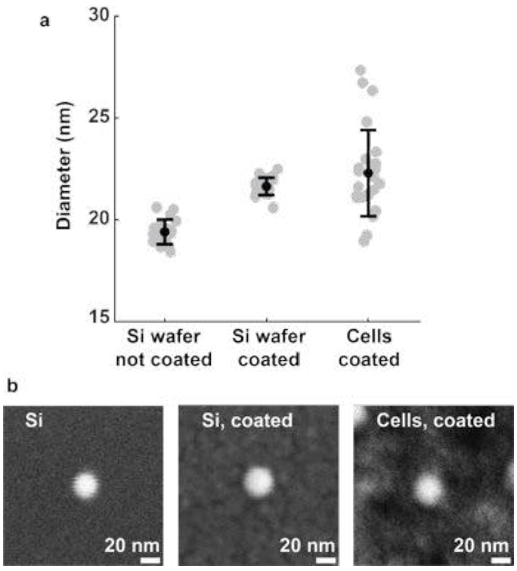

Supplementary Figure 38: Impact of sputter coating on LNP diameter. (a) Comparison of LNP diameters on Si substrate without sputter coating, and on Si substrate and mammalian cells after sputter coating 2.5-nm-thick layer of 80:20 Pt:Pd. At least 20 LNPs were imaged for each condition. **(b)** Example images of single LNPs for the conditions shown in (a). Error bars show the mean and standard deviation. Source data are provided as a Source Data file.

As expected, the apparent size in sputter-coated samples was larger. The measured size distributions were 19.4 ± 0.6 nm for LNPs on the Si substrate without coating, 21.6 ± 0.4 nm on the coated Si substrate, and 22.3 ± 2.1 nm on coated cells. The broader size distribution observed on coated cells was likely due to cellular features in the electron images which resulted in less precise size measurements. In contrast, no such features were present on the Si substrate. Hence, our fitting algorithm for LNP size was less precise in the presence of cellular features around the LNPs.

Supplementary Note 25. Impact of plasma on the brightness of LNPs

The results presented in **Fig. 5c** demonstrate that sputter coating could reduce the brightness of LNPs. We attributed this reduction in brightness to the exposure of LNPs to plasma during the sputter coating process. To test this hypothesis, we used a plasma cleaner to subject $NaHoF_4$ LNPs to varying durations of plasma exposure, but without sputter coating. Indeed, we observed a significant decrease in their brightness of LNPs (**Supplementary Figure 39**).

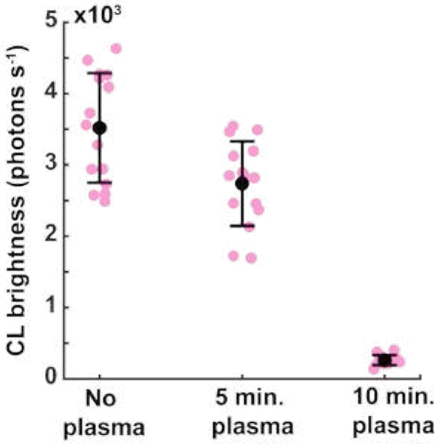

Supplementary Figure 39: Impact of plasma on CL brightness. CL brightness of $NaHoF_4$ LNPs under different exposures to plasma. The experiments were performed with a PE-25 plasma cleaner from Plasma Etch, Inc. 15 LNPs were imaged for each condition. Error bars show the mean and standard deviation. Source data are provided as a Source Data file.

Supplementary Note 26. Nonlocal excitation from the SEM chamber

In our initial single-particle experiments, we observed CL from samples containing only non-emitting $NaGdF_4$ nanocrystals. This was unexpected because these particles only emitted in the ultraviolet spectral range[16,17], which is filtered out by our emission-path optics and is not detected by the PMTs. The CL from these nanocrystals increased at shorter wavelengths (**Supplementary Figure 40a,c**).

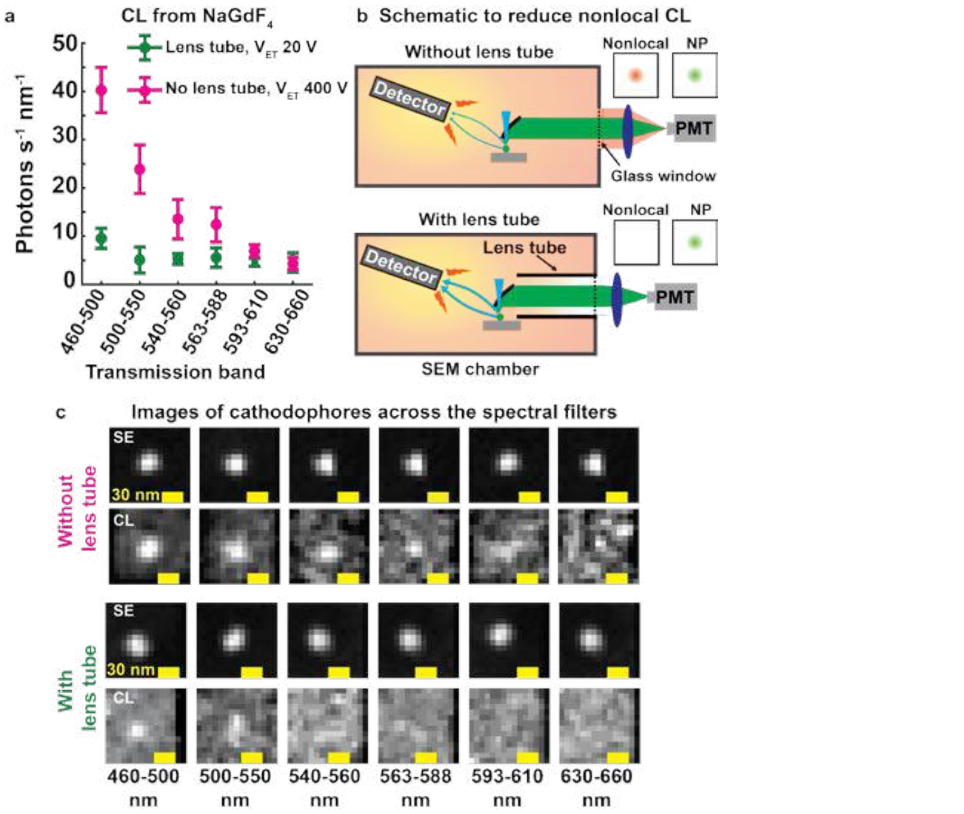

Supplementary Figure 40: Nonlocal CL signal from the Everhart-Thornley detector. (a) Rate of CL detection from non-luminescent $NaGdF_4$ nanocrystals across six spectral filters. The rate was normalized by the bandwidth of the filters. The rate is shown for two conditions: (i) without the lens tube and a voltage (V_{ET}) of 400 V on the Everhart-Thornley detector, and (ii) with the lens tube and a V_{ET} of 20 V on the detector. The lens tube was used to prevent light emitted by the scintillator of the detector from reaching the PMTs. 15 LNPs were imaged for each band. Error bars show the mean and standard deviation of the data. **(b)** A schematic showing nonlocal CL originating from the Everhart-Thornley detector upon excitation by electrons from the sample. This nonlocal CL was prevented from reaching the detector by optically isolating the emission path inside the SEM with a lens tube. The tube extended from the side port of the SEM to the parabolic mirror. **(c)** SE and CL images of non-luminescent $NaGdF_4$ nanocrystals across the spectral filters shown in (a), both without and with the lens tube. V_{ET} was 400 V and 20 V, respectively.

Investigating this phenomenon led us to conclude that this luminescence originated from the Everhart-Thornley detector that detects electrons using a luminescent scintillator (**Supplementary Figure 40b**). It is this luminescence that was detected when an $NaGdF_4$ nanocrystal was excited with the electron beam. Deceivingly, this luminescence could be interpreted as CL from the nanocrystals because it was only observed when the electron beam was scanning across a nanocrystal, thus forming its image in the short-wavelength CL channels (**Supplementary Figure 40c**). This is because the nanocrystal contained high-atomic-number (high Z) ions (Gd^{3+}) while the substrate was composed of light atoms (Si), so more stray electrons were generated when the electron beam was scanned across the nanocrystal, leading to larger electron signal and increased luminescence from the scintillator in the Everhart-Thornley detector. We have addressed this issue by reducing the Everhart-Thornley bias voltage from 400 V to 20 V and optically isolating the detection path using a lens tube as shown in **Supplementary Figure 40b**.

Supplementary Note 27. Dipole emission on different substrates

In our single-particle CL experiment, LNPs were placed on top of a Si substrate inside the SEM vacuum chamber, and the parabolic mirror collected light emitted into vacuum by the LNPs. To better understand the collection efficiency of the CL detection system, we used the

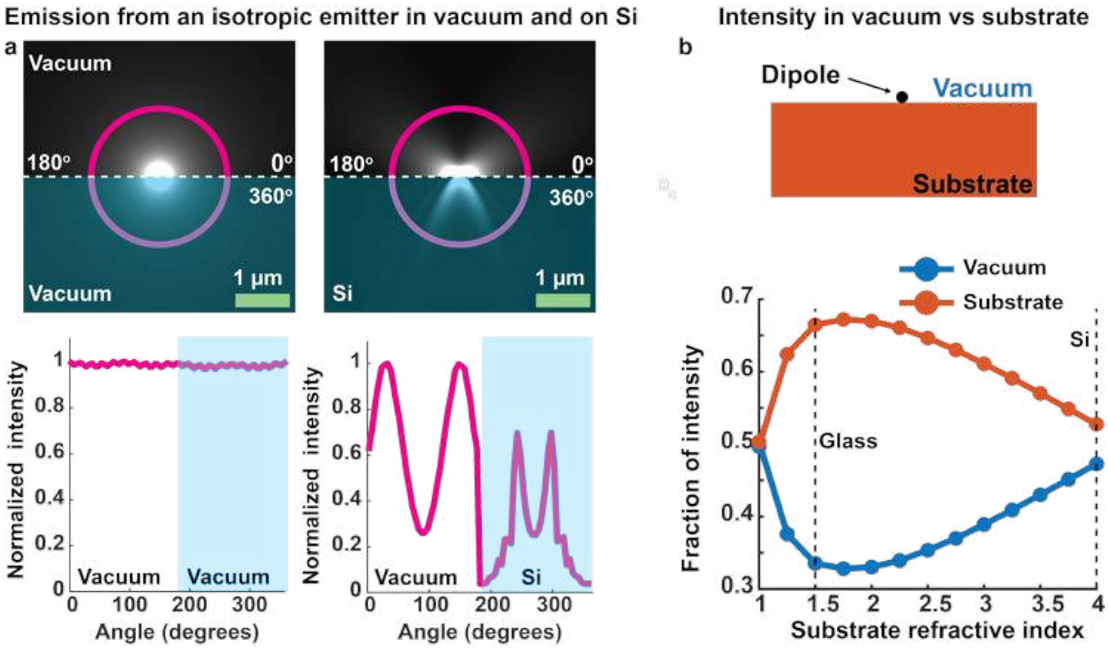

Supplementary Figure 41: Emission profiles from isotropic emitters on different sufaces. (a) Emission profile of an isotropic emitter placed in vacuum and at the Si-vacuum interface. **(b)** Fraction of intensity emitted into vacuum and the substrate for different refractive indices of the substrate. For analysis in (b), only the real part of the refractive index was considered. Simulations were performed using Lumerical FDTD. Source data are provided as a Source Data file.

FDTD solver in Lumerical software to perform electromagnetic simulations of an isotropic emitter placed at the Si-vacuum interface. In the absence of a Si substrate, an isotropic emitter emitted uniformly in all directions. However, the emission pattern changed when the emitter was placed on a substrate with a refractive index $n > 1$ (**Supplementary Figure 41a**).

Supplementary Figure 41b shows fractions of energy emitted upwards, i.e., into vacuum, and into the substrate for different refractive indices (n) of the substrate. The emission into vacuum did not decrease monotonically as a function of n. Instead, the energy directed into vacuum reached its minimum at $n \approx 1.7$, and increased with a further increase in n. For Si ($n \approx 4$), ≈47% of the total energy was emitted into vacuum. These simulations showed that for an isotropic emitter at a Si-vacuum interface, the fraction of energy directed into vacuum was not drastically different from the case in which there was no substrate (i.e., 50% for the isotropic $n = 1$ environment).

Supplementary Note 28. Repeatability

We investigated the consistency of CL signal from LNPs across different syntheses**.** **Supplementary Figure 42** shows the rate of CL detection as a function of size for LNPs obtained from four syntheses. The figure shows that the CL signal was consistent across the syntheses.

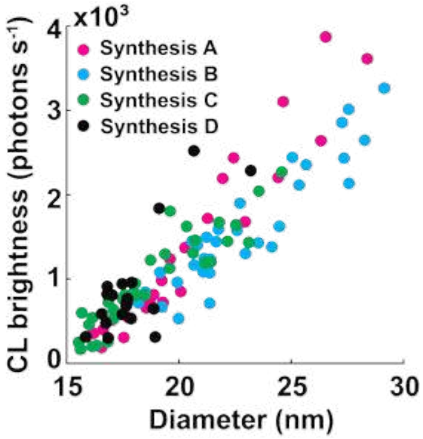

Supplementary Figure 42: Reproducibility of CL across LNP syntheses. CL detection rate from $NaHoF_4$ LNPs from different syntheses. No change in the detection rate was observed. CL was measured in the Ho^{3+} channel. Source data are provided as a Source Data file.

Supplementary Note 29. Crosstalk between LNPs in dense samples

<u>Simulations:</u> Fig. 3a shows results of Monte Carlo simulations performed to determine

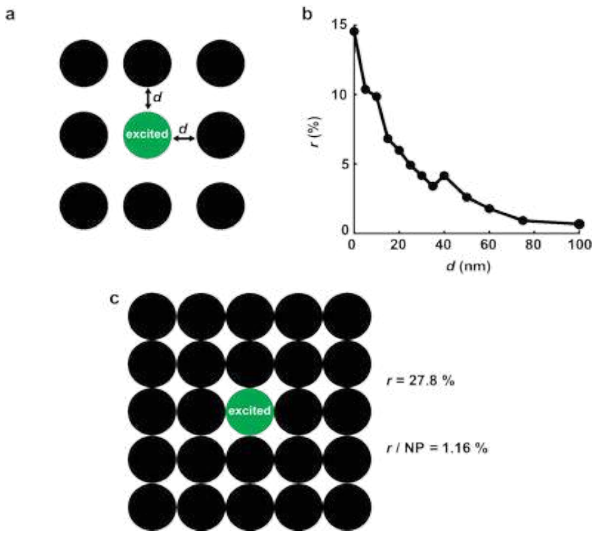

Supplementary Figure 43: Simulation of crosstalk in dense LNP samples. (a) Monte Carlo simulations for the configuration when an excited central nanocrystal (green) was surrounded by adjacent nanocrystals (black). The nanocrystals were $NaHoF_4$, with 20 nm diameter. Electron beam energy was 3 keV and 1,000 trajectories were simulated. **(b)** Total energy (relative to energy deposited in the central nanocrystal) deposited across all adjacent nanocrystals when the central nanocrystal was excited, shown as a function of the distance *d* between the central nanocrystal and adjacent nanocrystals.This relative energy was calcualted as: $r = \frac{\sum E_{adjacent}}{E_{excited}}$, where $\sum E_{adjacent}$ is the sum of energies absorbed by nanocrystals adjacent to the excited nanocrystal, and $E_{excited}$ is the energy absorbed by the excited nanocrystal. **(c)** Monte Carlo simulations for the configuration when an excited central nanocrystal was surrounded by 24 adjacent nanocrystals. 27.8% energy (relative to the central nanocrystal) was deposited in adjacent nanocrystals, corresponding to an average of 1.16% energy per nanocrystal. Source data are provided as a Source Data file.

crosstalk between two adjacent nanocrystals, each 20 nm in diameter. In this setup, the crosstalk was minimal. However, this simulation only considered two nanocrystals. Our multicolor imaging was performed in dense monolayers of LNPs. In such samples, the crosstalk could increase, particularly when a single LNP was surrounded by other LNPs of a different color. To understand the crosstalk in such a sample, additional Monte Carlo simulations were performed using CASINO software. Simulations were performed with $NaHoF_4$ LNPs of 20 nm diameter, and an electron beam energy of 3 keV. 1,000 trajectories were simulated for each condition.

Supplementary Figure 43a shows a situation where the excited nanocrystal (shown in green) was surrounded by eight other nanocrystals. We measured the energy deposited in the adjacent nanocrystals (shown in black) when the central nanocrystal was excited. The deposited energy was calculated at different distances, *d*, from the excited nanocrystal. Results are shown in **Supplementary Figure 43b.** The largest amount of energy was deposited into black nanocrystals for *d* = 0 nm, i.e., when the black nanocrystals were directly touching the green nanocrystal. In this scenario, ≈14.5% of energy, relative to the energy absorbed by the excited nanocrystal, was deposited in adjacent nanocrystals (≈1.8% energy per adjacent nanocrystal, consistent with **Fig. 3a**). When the distance increased to 25 nm, the absorbed energy decreased to ≈5%, or 0.63% per adjacent nanocrystal. We also performed a simulation with 24 nanocrystals surrounding the excited nanocrystal as shown in **Supplementary Figure 43c.** In this case, the energy deposited in the adjacent nanocrystals was 27.8%, or 1.16% per nanocrystal.

These simulations show that, even in dense samples where LNPs are in direct contact, the energy deposited in adjacent LNPs is not prohibitive. However, despite this minimal energy absorbed per neighboring LNP, if a single LNP is surrounded by multiple LNPs of a different color (e.g., $NaHoF_4$ surrounded by $NaDyF_4$), a detectable CL signal can appear in the wrong color channel. This potential crosstalk should be considered when classifying nanocrystals.

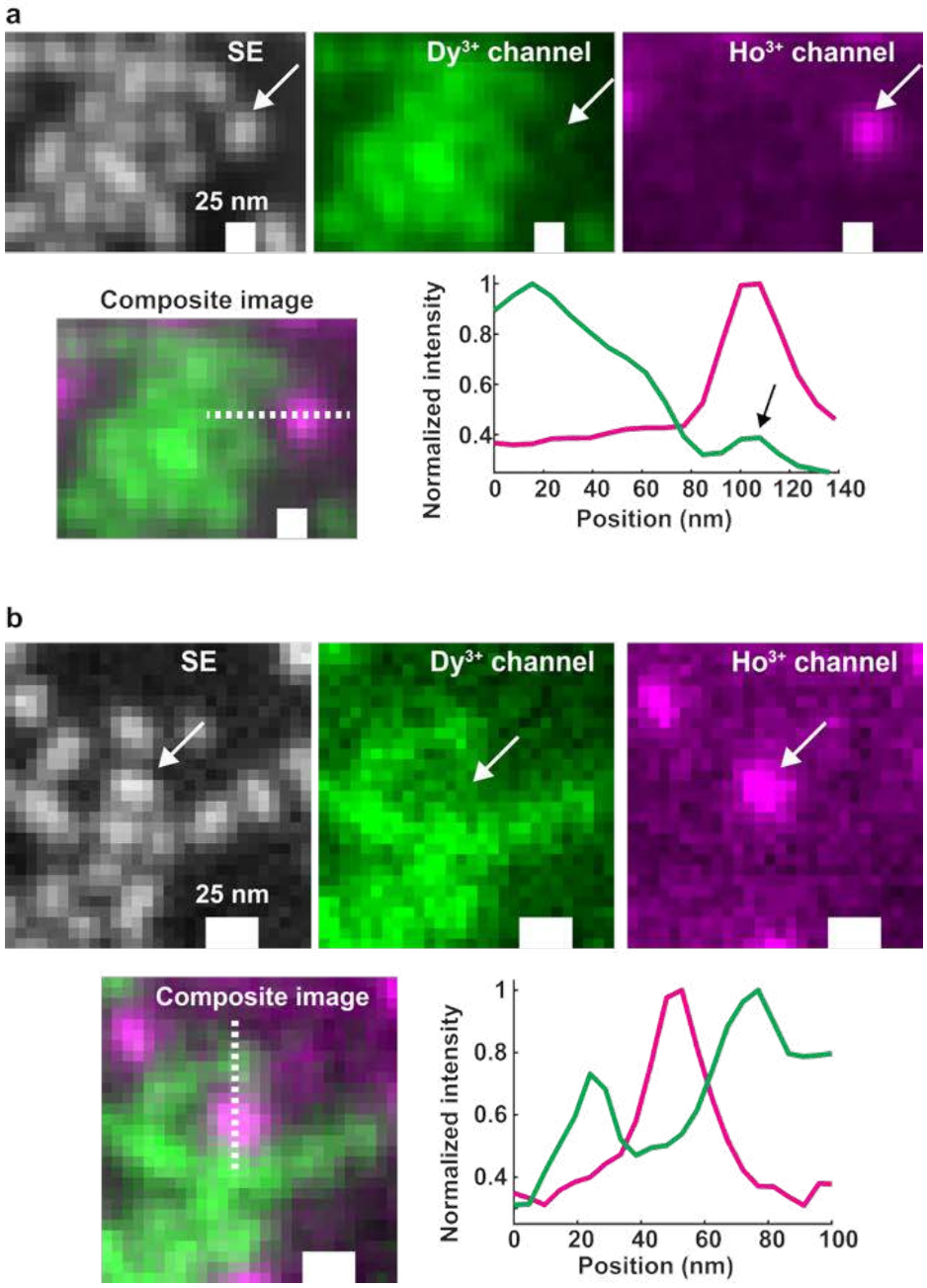

Supplementary Figure 44: Crosstalk in dense, non-aggregated samples. (a,b) Two examples of two-color imaging in a dense, monolayered sample, when a $NaHoF_4$ LNP was close to multiple $NaDyF_4$ LNPs. Crosstalk was minimal and the LNPs could be distinguished from their CL signal in the Ho^{3+} and Dy^{3+} color channels. Source data are provided as a Source Data file.

Experiment: **Supplementary Figure 44** shows two examples of two-color imaging when $NaHoF_4$ LNPs were imaged adjacent to multiple $NaDyF_4$ LNPs. In such a situation, some crosstalk was noticeable. For example, in **Supplementary Figure 44a** CL signal appeared in the Dy^{3+} color channel when a $NaHoF_4$ LNP was excited (see black arrow in the cross-sectional profile). However, because the excited LNP absorbed considerably more energy than the surrounding nanocrystals, we could classify all the LNPs in the FOV based on their emission in the two spectral channels.

Supplementary Note 30. Summary of imaging conditions from main text

The table below provides a summary of the imaging conditions for figures in the main text.

Figure	Frame dwell time (ms)	Other details
1a,d CL images	1	50 frames with 1 ms per frame
2b,c,e-j,l-n	1	50 frames with 1 ms per frame
3b-f	1	50 frames with 1 ms per frame
3g-j	0.1	321 frames with 0.1 ms per frame
3k-n	0.1	500 frames with 0.1 ms per frame
4c	1	50 frames with 1 ms per frame
5e,f	0.1	50 frames with 1 ms per frame

Supplementary Table 2: CL imaging conditions. Imaging conditions, i.e., beam dwell time and the number of captured frames for the CL experiments in the main text.

Supplementary References

1. Prigozhin, M. B. *et al.* Bright sub-20-nm cathodoluminescent nanoprobes for electron microscopy. *Nat. Nanotechnol.* **14,** 420–425 (2019).
2. Fischer, S., Bronstein, N. D., Swabeck, J. K., Chan, E. M. & Alivisatos, A. P. Precise tuning of surface quenching for luminescence enhancement in core–shell lanthanide-doped nanocrystals. *Nano Lett.* **16,** 7241–7247 (2016).
3. Shang, Y. *et al.* Low threshold lasing emissions from a single upconversion nanocrystal. *Nat. Commun.* **11,** 6156 (2020).
4. Wang, Z. & Meijerink, A. Concentration quenching in upconversion nanocrystals. *J. Phys. Chem. C Nanomater. Interfaces* **122,** 26298–26306 (2018).
5. Wen, S. *et al.* Advances in highly doped upconversion nanoparticles. *Nat. Commun.* **9,** 2415 (2018).
6. Lawrence Berkeley National Laboratory. X-Ray Properties of the Elements. https://xdb.lbl.gov/Section1/.
7. Lawrence Berkeley National Laboratory. X-Ray Attenuation Length. https://henke.lbl.gov/optical_constants/atten2.html.
8. Melle, S. *et al.* Förster resonance energy transfer distance dependence from upconverting nanoparticles to quantum dots. *J. Phys. Chem. C Nanomater. Interfaces* **122,** 18751–18758 (2018).
9. Cho, H.-H. *et al.* Suppression of Dexter transfer by covalent encapsulation for efficient matrix-free narrowband deep blue hyperfluorescent OLEDs. *Nat. Mater.* **23,** 519–526 (2024).
10. Wang, J. *et al.* Carrier recombination and plasmonic emission channels in metallic photoluminescence. *Nanoscale* **10,** 8240–8245 (2018).
11. van Wijngaarden, J. T. Cathodoluminescence imaging spectroscopy on plasmonic structures. (Institute AMOLF, 2005).
12. Tanuma, S., Powell, C. J. & Penn, D. R. Calculations of electron inelastic mean free paths. IX. Data for 41 elemental solids over the 50 eV to 30 keV range. *Surf. Interface Anal.* **43,** 689–713 (2011).

13. Drouin, D. *et al.* CASINO V2.42: a fast and easy-to-use modeling tool for scanning electron microscopy and microanalysis users. *Scanning* **29,** 92–101 (2007).
14. Tanida, I. *et al.* Two-color in-resin CLEM of Epon-embedded cells using osmium resistant green and red fluorescent proteins. *Sci. Rep.* **10,** 21871 (2020).
15. Schu, M. *et al.* Scanning electron microscopy preparation of the cellular actin cortex: A quantitative comparison between critical point drying and hexamethyldisilazane drying. *PLoS One* **16,** e0254165 (2021).
16. Wang, L. *et al.* Enhanced deep-ultraviolet upconversion emission of Gd3+ sensitized by Yb3+ and Ho3+ in β-NaLuF4 microcrystals under 980 nm excitation. *J. Mater. Chem.* **1,** 2485–2490 (2013).
17. Brixner, L. H. & Blasse, G. Gd3+ emission from the two crystallographic sites of C-type Y 2 O 3. *J. Electrochem. Soc.* **136,** 3529 (1989).